



The enhancement of CdS photocatalytic activity for water splitting via anti-photocorrosion by coating Ni₂P shell and removing nascent formed oxygen with artificial gill

Wenlong Zhen^{a,b}, Xiaofeng Ning^a, Baojun Yang^a, Yuqi Wu^{a,*}, Zhen Li^a, Gongxuan Lu^{a,*}

^a State Key Laboratory for Oxo Synthesis and Selective Oxidation, Lanzhou Institute of Chemical Physics, Chinese Academy of Science, Lanzhou 730000, China

^b University of Chinese Academy of Science, Beijing 100049, China

ARTICLE INFO

Keywords:

Inhibition of CdS photocorrosion
Core-shell structured Ni₂P@CdS
Visible light-driven
Overall water splitting
Artificial gill

ABSTRACT

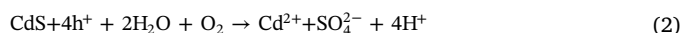
CdS photocorrosion seriously impeded its application in photocatalysis, especially for water splitting. Here we report new strategies to improve CdS photocorrosion resistance properties significantly by coating Ni₂P shell and assembling an artificial gill to remove newly formed O₂ from water. Ni₂P@CdS catalyst can achieve the over-all water splitting under visible light irradiation without addition of any sacrifice reagent and noble metal loading. Compared with CdS itself, the 10Ni₂P@CdS photocatalyst exhibits excellent photocatalytic activity for hydrogen evolution (251.4 μmol of H₂ in 180 min) with a high AQE (3.89% at 430 nm). This catalyst also presents high photocurrent, low overpotential (−0.32 V vs SCE), and long fluorescence lifetime (16.27 ns) of excited charges. Cd²⁺ ions concentration measured by ICP and long term stability results verified the anti-photocorrosion role of Ni₂P shell on CdS during water splitting reaction. The activity and stability of 10Ni₂P@CdS is even superior to typical 1Pt@CdS catalyst. Our results confirm CdS can be an active catalyst for photocatalytic hydrogen generation from water under visible irradiation if its stability is enhanced by protection of anti-photocorrosion over-coating shell and removing the nascent formed oxygen from water.

1. Introduction

Sustainable H₂ production from water via semiconductor photocatalysis driven by solar energy has been regarded as a viable solution to address the increasing environmental and energy issues [1–3]. Exploring efficient, enduring, low-cost, stable and nontoxicity photocatalysts for H₂ evolution reaction (HER) from water still remains a great challenge [4]. Most of these photocatalysts are only active under UV light, which accounts for only approximately 3%–5% of the solar spectrum on the surface of the earth, seriously restricting its solar efficiency [5–10]. To utilize sunlight source more efficiently, it is of significant importance to develop visible light-driven photocatalysts through the modification of wide-bandgap semiconductors or finding new visible light-driven photocatalysts. Recently, many visible light-driven photocatalysts (such as BiVO₄ [11], Ta₃N₅ [12], g-C₃N₄ [13,14], and CdS [15,16]) have also been reported. Among them, CdS possesses excellent photoelectrochemical performance due to its relatively narrow band gap (~2.4 eV) and appropriate band position, that meets the thermodynamic requirement for photocatalysis water splitting [17,18]. However, CdS itself has relatively low chemical stability under visible-light irradiation as it can be easily oxidized by O₂ [16].

To date, much works has been carried out to retard the photocorrosion of CdS nanoparticles (NPs). For instance, Su *et al.* reported that the PANI@CdS core-shell nanospheres exhibited enhanced anti-photocorrosion properties and photocatalytic hydrogen production activity [19]. Ikeue *et al.* have synthesized the composite sulfide catalyst (Mn_{1-x}Cd_xS) by a hydrothermal method and found that the photocatalytic activity of Mn_{1-x}Cd_xS is higher than that of single CdS [20]. Hu *et al.* indicated that carbon-coating over CdS could prevent CdS from oxidation [21]. Yang *et al.* found that, the GR–CdS–MoS₂ material displayed high photocatalytic activity for HER and anti-photocorrosion ability compared with pure CdS [22]. However, most of these works often invoke harsh synthesis conditions or require continuous feeding of sacrificial agents into the photocatalytic system.

The photocorrosion processes of CdS in the absence and presence of H₂O and O₂ can be described by Eqs. (1) and (2), respectively:



In fact, the photocorrosion is not only related to the photogenerated hole (h⁺) in semiconductor itself, but also related to the newly formed

* Corresponding authors.

E-mail addresses: wuyuqicas@163.com (Y. Wu), gxlul@lzb.ac.cn (G. Lu).

oxygen in the water [23]. In addition, since the dissolved oxygen is about 5 times higher than that of hydrogen in water, the reaction of hydrogen and oxygen recombination occurred very fast over the photocatalysts surface [24], which further inhibited the performance of catalyst for water splitting consequently. Domen and co-workers have previously achieved overall water splitting under visible light using $\text{LaMg}_{1/3}\text{Ta}_{2/3}\text{O}_2\text{N}$ modified with a metal oxyhydroxide layer [25], which could inhibit hydrogen and oxygen recombination reaction. Li *et al.* also indicated that the recombination of hydrogen and oxygen could be inhibited by addition of oxygen transfer reagent hemin chloride [26]. Inspired by the respiratory system of fish, the application of artificial gill in photocatalytic overall water splitting might remove neonatal formed O_2 from water and prevent the oxygen leading photocorrosion, as a result, the reverse reaction of hydrogen and oxygen recombination back to water could be retarded.

Another important challenge is replacement noble metal co-catalyst in photocatalysis by earth abundant elements because Pt-group metals are scarceness and high-cost [27], for example by transition-metal phosphides, which exhibited noble-metal-like properties for HER [28–35]. Herein, we develop core-shell structured $\text{Ni}_2\text{P}@ \text{CdS}$ photocatalyst by solvothermal method for high efficient HER under visible light irradiation without sacrifice reagent and noble metal loading. With help of artificial gill removing newly formed O_2 from water, the oxygen leading photocorrosion was prevented and the hydrogen and oxygen recombination to water was inhibited. Compared with CdS itself, $\text{Ni}_2\text{P}@ \text{CdS}$ core-shell photocatalyst exhibits excellent photocatalytic activity for water splitting. Characterization results further indicate the Ni_2P shell over CdS surface can inhibit CdS from photocorrosion. More importantly, Ni_2P co-catalyst is a promising substitute for replacement of noble-metals in photocatalytic HER.

2. Experimental methods

2.1. Materials

All chemicals were commercial purchased and used without further purification. Cadmium nitrate ($\text{Cd}(\text{NO}_3)_2 \cdot 4\text{H}_2\text{O}$, Tianjin Kemiou Chemical Reagent Co., Ltd, AR, $\geq 99.0\%$), sodium sulfide ($\text{Na}_2\text{S} \cdot 9\text{H}_2\text{O}$, Chengdu Kelong Chemical Reagent Co., Ltd, AR, $\geq 98.0\%$), chloroplatinic acid ($\text{H}_2\text{PtCl}_6 \cdot 6\text{H}_2\text{O}$, Tianjin Kemiou Chemical Reagent Co., Ltd, AR, $\geq 99.0\%$), ethylenediamine ($\text{NH}_2\text{CH}_2\text{CH}_2\text{NH}_2$, Shanghai Aladdin Bio-Chem Technology Co., Ltd, $> 99.0\%$), thioacetamide (CH_3CSNH_2 , Sinopham Chemical Reagent Co., Ltd, AR, $\geq 99.0\%$), hydrazine hydrate ($\text{H}_4\text{N}_2 \cdot \text{H}_2\text{O}$, Xilong Chemical Co., Ltd., AR, $> 80\%$), nickelnitrate ($\text{Ni}(\text{NO}_3)_2 \cdot 6\text{H}_2\text{O}$, AR, J & K Scientific Ltd., $\geq 96.0\%$), phosphorus white (P_4 , Sinopham Chemical Reagent Co., Ltd, AR, $\geq 99.8\%$), benzene (C_6H_6 , Tianjin Kemiou Chemical Reagent Co., Ltd, AR, $\geq 99.0\%$), deuterioxide (D_2O , J & K Scientific Ltd., AR, $> 99\%$), water- ^{18}O (H_2^{18}O , J & K Scientific Ltd., AR, $> 97\%$), ethanol ($\text{C}_2\text{H}_5\text{OH}$, Xilong Chemical Co., Ltd., $> 99.8\%$), sodium sulfate anhydrous (Na_2SO_4 , Xilong Chemical Co., Ltd, AR, $\geq 99\%$), potassium hydroxide

(KOH, Xilong Chemical Co., Ltd, AR, $\geq 99\%$), potassium bromate (KBrO_3 , Xilong Chemical Co., Ltd, AR, $\geq 99\%$), 5,5-dimethyl-1-pyrrolineN-oxide (DMPO, J & K Scientific Ltd., $\geq 98.0\%$). De-ionized water with a specific resistance of $18.2 \text{ M}\Omega \text{ cm}$ was obtained by reverse osmosis followed by ion-exchange and filtration (Milli-Q™ Advantage A10™, France). All of the reagents were used in the experiments.

2.2. Catalyst preparation

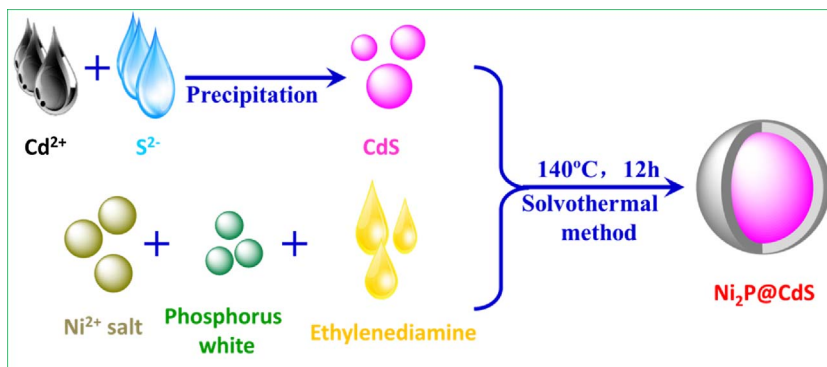
2.2.1. Synthesis of CdS and CdS-H samples

CdS sample was prepared by a typical precipitation method. Briefly, 3.5 mmol (1.0797 g) $\text{Cd}(\text{NO}_3)_2 \cdot 4\text{H}_2\text{O}$ was dissolved in 20 mL of deionized water and stirred vigorously for 60 min, 7.0 mmol (1.6813 g) $\text{Na}_2\text{S} \cdot 9\text{H}_2\text{O}$ was dissolved into another 10 mL of deionized water by ultrasonication to obtain the Na_2S solution. Then the Na_2S solution was slowly added into the above-mentioned $\text{Cd}(\text{NO}_3)_2$ solution in a drop-by-drop process under vigorous stirring. After stirring for 3 h, the obtained yellow precipitate was filtrated, washed with deionized water several times, and dried at 80°C for 12 h. Finally, the products were collected and ground into powder by an agate mortar for further use.

For comparison, the small-sized CdS catalyst was also synthesized by hydrothermal method [36]. CdS nanocrystal was prepared by sequentially adding 5 mL of ethylenediamine and 12.5 mmol (0.9391 g) of thioacetamide to a 20 mL aqueous solution containing 5 mmol (1.5424 g) of cadmium nitrate. The volume of the reaction solution was adjusted to be 30 mL by introducing additional water. The entire process was carried out under magnetic stirring. The reaction mixture was further stirred for 20 min, sealed in a 50 mL capacity Teflon-lined autoclave, and heated to 230°C at a ramping speed of $30^\circ\text{C min}^{-1}$ in the presence of microwave irradiation. The reaction was allowed to proceed for 30 min. After cooling, the product was separated by centrifugation, washed several times with deionized water and ethanol, and dried at 80°C for 5 h in a vacuum oven. Finally, the products were collected and ground into powder by an agate mortar for further use. The synthesized CdS catalysts by precipitation and hydrothermal methods were denoted as CdS and CdS-H, respectively.

2.2.2. Synthesis of Ni_2P

The Ni_2P was successfully prepared through a simple solvothermal process according to the previous literatures [37]. Typically, 0.7270 g (2.5 mmol) $\text{Ni}(\text{NO}_3)_2 \cdot 6\text{H}_2\text{O}$ and 1.5487 g (12.5 mmol) phosphorus white were put into an 100 mL autoclave with Teflon liner, which was then filled with ethylenediamine up to 80% of its capacity. The mixture was sonicated for about 20 min until it became homogeneous. The autoclave was maintained at 140°C for 12 h and then cooled to room temperature naturally. The black precipitates were collected and washed with benzene, ethanol, and distilled water in sequence to remove the byproducts and possible impurities. The final products were dried in vacuum at 60°C for 12 h.



Scheme 1. Schematic illustration on the synthesis of $\text{Ni}_2\text{P}@ \text{CdS}$ core-shell structure sample.

2.2.3. Synthesis of $x(\text{wt.}\%)\text{Ni}_2\text{P}@ \text{CdS}$ and $10\text{Ni}_2\text{P}@ \text{CdS-H}$ samples

The core-shell structure of $x\text{Ni}_2\text{P}@ \text{CdS}$ samples were prepared by solvothermal method (Scheme 1) [38]. The Ni_2P loading was $x\%$ ($x = 1, 2.5, 5, 10, 15$ and 20) and denoted as $x\text{Ni}_2\text{P}@ \text{CdS}$. Typically, taking $10\text{Ni}_2\text{P}@ \text{CdS}$ catalyst as an example, 0.1568 g (0.54 mmol) of $\text{Ni}(\text{NO}_3)_2 \cdot 6\text{H}_2\text{O}$, 0.3343 mg (2.7 mmol) of phosphorus white, 0.3600 g (2.5 mmol) of CdS were suspended in 80 mL of ethylenediamine and the mixture was sonicated for about 20 min until it became homogeneous. The mixed solution was then transferred into an autoclave with an inner Teflon lining and maintained at 140°C for 12 h . After that, the precipitate was collected by centrifugation, washed with benzene, ethanol and distilled water three times, and then dried in vacuum at 60°C for 12 h .

The synthetic method of $10\text{Ni}_2\text{P}@ \text{CdS-H}$ was the same as $10\text{Ni}_2\text{P}@ \text{CdS}$ sample. The cadmium sulfide of hydrothermal method (CdS-H) was selected as support for $10\text{Ni}_2\text{P}@ \text{CdS-H}$ catalyst.

2.2.4. Synthesis of $x(\text{wt.}\%)\text{Pt}@ \text{CdS}$ samples

The $x\text{Pt}@ \text{CdS}$ samples were prepared by *in-situ* impregnation-reduction method according to the latest reports [39,40]. The Pt loading was $x\%$ ($x = 0.1, 0.25, 0.5, 1, 1.5$ and 2) and denoted as $x\text{Pt}@ \text{CdS}$. As an example of $1\text{Pt}@ \text{CdS}$, 0.1980 g CdS was dispersed in water (10 mL). The dispersion solution was sonicated for about 20 min until it became homogeneous. 1.125 mL H_2PtCl_6 solution (9.1 mmol/L) was added to the above-mentioned CdS dispersion solution. The mixture was stirred in half an hour, and then a calculated amount of hydrazine hydrate was dropped into the solution. After complete reduction, the obtained dispersions were filtered, washed with water several times to remove the impurities ion. Finally, the obtained wet solids were dried in vacuum at 80°C for 12 h .

2.3. Photocatalytic activities measurement

Photocatalytic experiments were performed at room temperature in a sealed Pyrex flask (231 mL) with a flat window (an efficient irradiation area of 9.8 cm^2) and a silicone rubber septum for sampling. 100 mg of catalyst was dispersed into 150 mL H_2O under the ultrasound treatment (25 kHz , 250 W) about 10 min . Prior to irradiation, the reactant mixture was degassed by bubbling Ar gas for 40 min . The Xenon lamp (HSX-UV 300, NBeT) with a 420 nm cut-off filter was used as a light source to trigger the photocatalytic reaction and was positioned 15 cm away from the reactor. The amount of hydrogen evolution was measured using gas chromatograph (Agilent 6820, TCD, 13 X columns, Ar carrier). A continuous magnetic stirrer was applied at the bottom of the reactor in order to keep the photocatalyst in suspension status during the whole experiment.

The apparent quantum efficiency (AQE) was measured under the same photocatalytic reaction conditions with irradiation light through a bandpass filter ($430, 460, 490, 520$, or 550 nm). Photon flux of the incident light was determined using a Ray virtual radiation actinometer (FU 100, silicon ray detector, light spectrum, $400\text{--}700 \text{ nm}$; sensitivity, $10\text{--}50 \text{ V mmol}^{-1} \text{ m}^{-2} \text{ s}^{-1}$). The reaction solutions were irradiated for 30 min with bandpass filters for AQE tests on the H_2 production. The following Eq. (3) was used to calculate the AQE.

$$\text{AQE} = \frac{2 \times \text{the number of evolved hydrogen molecules}}{\text{the number of incident photons}} \times 100\% \quad (3)$$

The recycling test of photocatalytic H_2 evolution over the catalyst was done as follows. Typically, after the photocatalytic reaction of the first run under visible light irradiation, the photocatalytic system was thoroughly degassed again, without the separation of photocatalysts. Subsequently, the thoroughly degassed system was irradiated again by a 300 W Xe lamp with a 420 nm cut-off filter. Analogously, the following runs of photocatalytic recycling tests were performed.

2.4. Photocatalytic splitting D_2O and H_2^{18}O isotope-labeled experiments

The isotopes tracer experiments have been performed under downsizing the experimental conditions of photocatalytic splitting H_2O . Typically, 10 mg catalyst dispersed in 10 mL D_2O or 1 mL H_2^{18}O in the sealed Pyrex flask. After ultrasonic treatment for 30 min , the suspended aqueous solution is degassed by bubbling Ar gas for another 40 min . After visible light irradiation for 6 h , the gas mixture in container was measured by GC-MS (MAT 271). According to the NIST mass spectral database, the gas products were deduced from MS/MS mode and analyzed by scan mode.

2.5. Electrochemical measurements

All the electrochemical measurements were measured on an electrochemical analyzer (CHI660E) in a homemade standard three-electrode quartz cell consisting of an organic glass enclosure with a quartz window and a 1.2 cm diameter opening opposite the window to the work electrode was clamped. The working electrode was prepared by drop-coating sample suspensions directly onto the precleaned indium tin oxide glass (ITO glass) surface. Platinum plate was used as the counter electrode and a saturated calomel electrode (SCE) as the reference electrode. The electrolyte was 1 mol/L KOH aqueous solution without any additives. The visible light irradiation source was a 300 W Xe arc lamp system equipped with a 420 nm cut-off filter. The surface area of the working electrode exposed to the electrolyte was about 0.95 cm^2 . The cathodic polarization curves were obtained using the linear sweep voltammetry (LSV) technique with a scan rate of 1 mV s^{-1} . Moreover, to evaluate the flat-band potential (V_{fb}) of CdS , Ni_2P , $1\text{Pt}@ \text{CdS}$ and $10\text{Ni}_2\text{P}@ \text{CdS}$ samples Mott–Schottky plots at a frequency of 1 kHz were measured in 0.5 mol/L Na_2SO_4 electrolyte using a standard potentiostat equipped with an impedance spectra analyzer in the same electrochemical configuration and electrolyte under the dark condition. The measured potentials vs SCE were converted to the normal hydrogen electrode (NHE) scale by $E_{\text{NHE}} = E_{\text{SCE}} + 0.24$.

2.6. Characterization of the catalysts

The powder X-ray diffraction patterns (XRD) of the samples were recorded on a Rigaku B/Max-RB X-ray diffractometer with a nickel-filtered $\text{Cu K}\alpha$ radiation in the 2θ ranging from 10 to 80° and a position sensitive detector using a step size of 0.017° and a step time of 15 s at 40 mA and 40 kV . X-ray photoelectron spectroscopy (XPS) analysis was performed using a VG Scientific ESCALAB 250Xi-XPS photoelectron spectrometer with an $\text{Al K}\alpha$ X-ray resource. The binding energies were calibrated by the $\text{C} 1\text{s}$ binding energy of 284.7 eV . The specific surface areas of the catalysts were determined by N_2 adsorption-desorption measurements by employing the Brunauer-Emmet-Teller (BET) method (Micromeritics apparatus ASAP 2020 M) at 77 K . Transmission electron microscopy (TEM) and HRTEM images were taken with a Tecnai-G2-F30 field emission transmission electron microscope operating at accelerating voltage of 300 kV . Elemental mapping was performed by using an energy-dispersive X-ray spectrometer (EDS) attached to the TEM instrument. Ultraviolet-visible (UV-vis) diffuse reflectance spectra (DRS) were obtained with a Hewlett-Packard 8453 spectrophotometer in which BaSO_4 powder was used as the internal standard to obtain the optical properties of the samples. The photoluminescence (PL) spectra for samples were investigated on an Edinburgh FL/FS900 spectrophotometer with an excitation wave-length of 405 nm . The amount of Cd^{2+} in the reaction supernatant liquid resulting from photocorrosion was analysed by inductively coupled plasma-optical emission spectrometer (ICP, Agilent 725-ES) unit. The ICP signal intensities were calibrated by using a Cd elemental ICP standard solution. Electron paramagnetic resonance (EPR) of radicals trapped by 5, 5-dimethyl-1-pyrroline N-oxide (DMPO) was recorded on a Bruker EPR A200

spectrometer. The 0.1 mg/mL sample was vacuumed following by ventilated with argon for 3 times. After that, the sample was introduced into home-made quartz cup inside the microwave cavity and illuminated with a 300 W Xe lamp. The settings for the EPR spectrometer were as follows: center field, 3486.70 G; sweep width, 100 G; microwave frequency, 9.82 GHz; modulation frequency, 200 kHz; power, 20.00 mW. Magnetic parameters of the radicals detected were obtained from direct measurements of magnetic field and microwave frequency.

2.7. Artificial gill

It is known that fish can extract the dissolved oxygen from the water through the gill in the water [40]. Gill is a typical respiratory organ of fish, which consists of gill arch, gill rake, gill filament, gill lamella, etc. Fish exchanges the gas by gill lamella in the water. Gill wall is very thin, and contains a lot of capillaries. In the gill, the dissolved oxygen in the water is first absorbed by the capillaries, and the carbon dioxide is exchanged into the water in the mean time. One can achieve similar function just using a gas diffusion polymer film, one side is in water with dissolved oxygen and another side is bubbled with high pure argon gas. By this way, the oxygen concentration difference leads to oxygen diffusion from water side to the gas side, then the dissolved oxygen in water could be transferred from reaction mixture to gas phase. Actually this technique has been used to get oxygen from water, and the equipment is called artificial gill. We apply artificial gill to the photocatalytic overall water splitting system. The continuous argon gas was injected to decrease oxygen concentration in gas side of separation membrane, thus the dissolved oxygen would penetrate the separation membrane and was moved out of the reaction system.

3. Results and discussion

3.1. Photocatalytic performance

The photocatalytic overall water splitting performances for H_2 evolution were evaluated under visible light irradiation ($\lambda \geq 420$ nm) in a reactor equipped with an artificial gill, which could remove the oxygen dissolved in the dispersion out of the reactor. Fig. 1 showed the photocatalytic H_2 evolution amount over CdS, Ni_2P , $1Pt@CdS$, $10Ni_2P@CdS$ and $Ni_2P + CdS$ samples. Clearly, it could be noted that the $10Ni_2P@CdS$ photocatalyst had higher photocatalytic activity than other photocatalysts. Specifically, the $1Pt@CdS$ only gave $8.7 \mu\text{mol}$ of H_2 after 180 min of irradiation. $39.4 \mu\text{mol}$ and $59.8 \mu\text{mol}$ of H_2 were produced after 180 min of irradiation in the Ni_2P and $Ni_2P + CdS$ samples, respectively. This further suggested that, compared with Pt, the Ni_2P was the effective HER co-catalyst and more beneficial to H_2

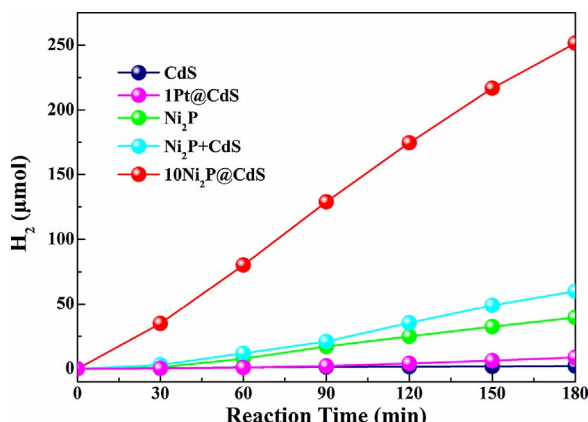


Fig. 1. Time courses of photocatalytic overall water splitting for hydrogen evolution over CdS, Ni_2P , $1Pt@CdS$, $10Ni_2P@CdS$ and $Ni_2P + CdS$ photocatalysts in 150 mL pure H_2O under visible-light irradiation ($\lambda \geq 420$ nm).

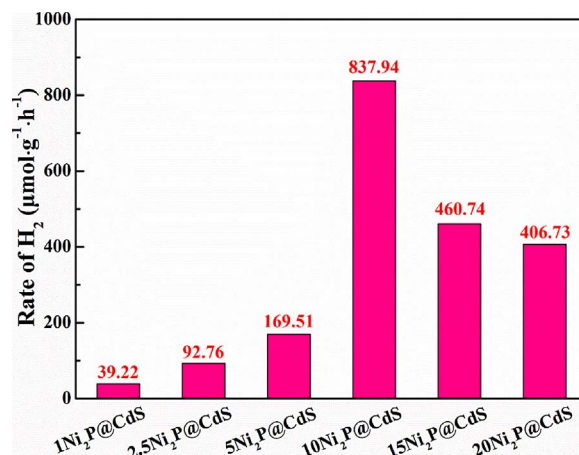


Fig. 2. Comparison of the photocatalytic splitting pure H_2O activity for different Ni_2P loading of xNi_2P/CdS samples under visible light irradiation ($\lambda \geq 420$ nm).

generation of photocatalytic water splitting. Here, $251.4 \mu\text{mol}$ of H_2 was evolved over the $10Ni_2P@CdS$ in 180 min, which was 28.7 times higher than that of $1Pt@CdS$ ($8.7 \mu\text{mol}$) under the same reaction conditions. It is known that Pt is a very good co-catalyst for HER. That activity of $10Ni_2P@CdS$ is superior to $1Pt@CdS$, mainly due to their noble-metal-like properties of transition metal phosphides (Ni_2P) [28–34,41].

Fig. 2 presented the HER activities of different Ni_2P loading of xNi_2P/CdS ($x = 1, 2.5, 5, 10, 15$ and 20) catalysts for the overall water splitting under visible light irradiation. Obviously, the sample loaded with 10% Ni_2P possessed the highest H_2 evolution activity and the rate of H_2 formation ($837.94 \mu\text{mol h}^{-1} \text{g}^{-1}$). The rate of H_2 evolution increased with Ni_2P loading increasing (from 1 to 10%), and a decay of the rate was observed with further increasing the Ni_2P loading amount (above 10%). Higher Ni_2P loading might provide more active sites, however, over loading resulted in the aggregation of surface Ni_2P , which would finally make the photocatalytic activity decrease.

Moreover, the rate of hydrogen was investigated over different Pt loading of $xPt@CdS$ photocatalysts (as shown in Fig. S1). Apparently, when the Pt loading increased, the HER rate increased and reached the maximum ($29.1 \mu\text{mol h}^{-1} \text{g}^{-1}$) at 1% Pt loading, then the rate began to decrease when Pt loading increase further. All of the $xNi_2P@CdS$ samples exhibited better photocatalytic H_2 production activity than $xPt@CdS$, and the sample of $10Ni_2P@CdS$ had the best activity. Fig. S2 displayed the photocatalytic activity over CdS and $Ni_2P@CdS$ with support of different preparation method. It was shown that the activities of CdS and $Ni_2P@CdS$ samples were higher than that of CdS-H and $Ni_2P@CdS$ -H, which was due to the different preparation method of CdS and CdS-H.

3.2. XRD, BET, and XPS analysis

In order to investigate the influence of surface structure on catalytic performance, the crystal structures of CdS, CdS-H, Ni_2P , $10Ni_2P@CdS$ and $1Pt@CdS$ photocatalysts were characterized by XRD technique, the results were given in Fig. 3. It is clear that the diffraction peaks of the CdS sample could be indexed to the cubic CdS phase (JCPDS# 10-0454). The peaks at 26.5° , 43.9° and 52.1° are attributed to the diffraction of the (111), (220) and (311) crystal planes of cubic CdS, respectively [42]. The XRD pattern of CdS-H are quite similar and could be all assigned to the hexagonal phase of pure cadmium sulfide by comparison with the standard data from JCPDS# 41-1049 [43]. The peaks at 40.7° , 44.6° , 47.4° , 54.2° and 55.0° over pure Ni_2P and $10Ni_2P@CdS$ belongs to the (111), (201), (210), (300), and (211) planes of hexagonal Ni_2P phase (JCPDS# 74-1385), respectively [31,44,45]. The XRD data of $10Ni_2P@CdS$ clearly shows the characteristic diffraction peaks of

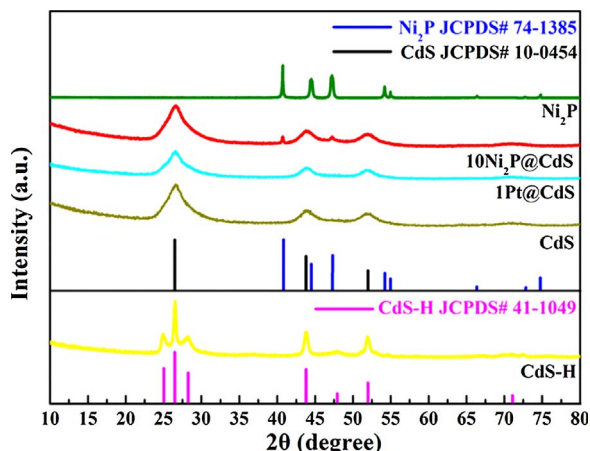


Fig. 3. XRD patterns of the CdS, CdS-H, Ni₂P, 10Ni₂P@CdS and 1Pt@CdS catalysts in the 2θ range from 10 to 80°.

Ni₂P and CdS, confirming that Ni₂P has been successfully loaded on the CdS. No diffraction peaks characteristic of Pt over 1Pt@CdS is observed because of its small particle size and low loading amounts [46,47].

The Brunauer–Emmett–Teller specific surface areas (S_{BET}) were determined by N₂ isotherms at 77 K (as shown in Table 1). The S_{BET} of CdS, CdS-H, Ni₂P, 1Pt@CdS and 10Ni₂P@CdS are 107.5, 51.8, 5.9, 63.0 and 87.4 m² g^{−1}, respectively. Compared with 1Pt@CdS, 10Ni₂P@CdS sample manifested the higher S_{BET} and pore volume, which would be beneficial to provide more active site for photocatalytic H₂ formation. In addition, the normalized per surface area of the photocatalytic activity have been present in Fig. S3. It was found that the 10Ni₂P@CdS photocatalyst had higher photocatalytic activity than 1Pt@CdS after the normalized. Specifically, the 1Pt@CdS only gave 0.139 μmol/(m² g^{−1}) of H₂ after 180 min of irradiation. However, 2.88 μmol/(m² g^{−1}) of H₂ was evolved over the 10Ni₂P@CdS in 180 min, which was 20.7 times higher than that of 1Pt@CdS under the same reaction conditions. Obviously, the surface area of the material is not dominant factor for activity.

To gain further insight of the surface composition of CdS, Ni₂P, 1Pt@CdS and 10Ni₂P@CdS catalysts, XPS technique was employed. Fig. 4a and b displayed the high-resolution spectra of the Cd 3d and S 2p regions, respectively. In Fig. 4a, the binding energies at 405.1 and 411.9 eV were assigned to the characteristic peaks of Cd 3d_{3/2} and Cd 3d_{5/2}, respectively, indicative of Cd²⁺ in catalysts. More importantly, a spin–orbit separation of 6.8 eV between Cd 3d_{3/2} and Cd 3d_{5/2} could further confirm the existence of Cd²⁺ on the surface of CdS nanoparticles [48]. Fig. 4b denoted the XPS spectrum of S 2p, the peaks located at 162.7 and 161.5 eV could be ascribed to the characteristic peaks of S 2p_{1/2} and S 2p_{3/2} spin-orbit components of S^{2−}, respectively, further implied that S^{2−} was the main existing form on the surface of CdS, 1Pt@CdS and 10Ni₂P@CdS samples for S element [49]. Fig. 4c and d showed the Ni 2p_{3/2} and P 2p XPS spectra of 10Ni₂P@CdS catalyst. In all cases, the contribution assigned to Ni^{δ+} at 853.5 eV (Ni₂P

Table 1
Structural parameters obtained from N₂ adsorption isotherms analysis.

Samples	S_{BET} (m ² g ^{−1}) ^a	Pore volume (cm ³ g ^{−1}) ^b	Average pore size (nm) ^b
CdS	107.5	0.2887	10.74
CdS-H	51.8	0.2464	19.01
Ni ₂ P	5.9	0.0242	16.48
1Pt@CdS	63.0	0.1179	7.49
10Ni ₂ P@CdS	87.4	0.1762	8.06

^a Obtained from BET method.

^b Total pore volume taken from the N₂ adsorption volume at a relative pressure (P/P₀) of 0.99.

phase) was observed and also that of Ni²⁺ due to superficial passivation, at 856.2 eV [50]. The binding energies at ~859.8 eV could be ascribed to the shoulder peak of Ni 2p_{3/2} [51,52]. Similarly, the high-resolution P 2p spectrum (as shown in Fig. 4d) can be fitted by three sub-peaks; the peaks centered at 129.8 (P 2p_{3/2}) and 130.7 eV (P 2p_{1/2}) might be assigned to P^{δ−} in the form of metal phosphide [53], and the peak at 134.3 eV was typical of oxidized phosphate species (PO₄^{3−}), likely due to superficial passivation of phosphide particles [54,55]. In Fig. 4e, the binding energies of 71.2 and 74.5 eV were associated with Pt 4f_{7/2} and Pt 4f_{5/2}, respectively, demonstrating that the Pt precursors could be reduced to metallic Pt over 1Pt@CdS sample. Fig. 4f showed XPS survey (wide-scan) spectra confirmed the existence of Cd, S, Ni and P elements over 10Ni₂P@CdS. The Cd 3d and S 2p XPS spectra of hydrothermal method catalyst CdS-H were given in Fig. S4a and b, respectively. Clearly, Cd²⁺ and S^{2−} over CdS-H were the main existing form on the surface of hexagonal CdS phase. The results were in good agreement with the previous reference [56].

3.3. TEM, UV–vis DRS, and Mott–Schottky analysis

To better understand the structure and morphology of CdS-H and CdS in the catalysts, the characterization data of scanning electron microscopy (SEM) and transmission electron microscopy (TEM) images of CdS-H and CdS were carried out and the results were shown in Fig. 5. In Fig. 5a–d, the SEM and TEM images indicate spherical and rodlike morphology for the as-synthesized samples of CdS and CdS-H, which is similar to the results of previous reports [42,57]. Analysis of high-resolution TEM (HRTEM) images of the CdS nanocrystal indicated that the d-spacing between two adjacent lattice planes are about 0.336 and 0.359 nm (as shown in Fig. 5e and f). These values are in good agreement with the spacing of CdS (111) and CdS-H (100) planes of face-centered cubic and hexagonal structure, respectively. Moreover, the structure and morphology of 10Ni₂P@CdS and 1Pt@CdS catalysts was studied by TEM technique. It is found that the as-synthesized 10Ni₂P@CdS show a core-shell structure with a uniform size of ~50 nm (see Fig. 6a). D-spacing fringes of 0.336 nm matching (111) planes of face-centered cubic CdS and d-spacing fringes of 0.221 nm matching the (111) planes of hexagonal Ni₂P are also observed in the HRTEM image (Fig. 6c). The energy-dispersive X-ray spectrum (EDX) measurement reveals the co-existence of Cd, S, P, and Ni elements in 10Ni₂P@CdS core-shell structure catalyst (Fig. 6e). The high-angle annular dark field scanning transmission electron microscopy (HAADF–STEM) imaging and EDX elemental mapping of 10Ni₂P@CdS clearly illuminate that the distribution of Cd, S, P, and Ni elements are relatively homogeneous in 10Ni₂P@CdS (Fig. 6g). These results are in good agreement with the results of XRD. However, the distribution of Pt is not very uniform over 1Pt@CdS catalyst surface by hydrazine hydrate assisted reduction (Fig. 6b). The lattice fringes with d-spacing 0.229 nm correspond to the (111) planes of Pt are also observed in the HRTEM image (Fig. 6d). Based on the EDX (Fig. 6f) and elemental mapping (Fig. 6h) data, further imply the co-existence of Cd, S, and Pt elements in 1Pt@CdS sample.

Fig. 7 presented the UV–vis diffuse reflectance spectra (DRS) of CdS, CdS-H, 1Pt@CdS and 10Ni₂P@CdS samples, which were widely used to measure the optical properties of semiconductor materials. It could be noted that the loading Ni₂P sample showed the band gap narrowing trend, i.e., red shift to higher wavelength, compared with pure CdS powder, which was evidenced by the plot of transformed Kubelka–Munk function vs the energy of light. As shown in the inset of Fig. 7, the band gaps of CdS, CdS-H, 1Pt@CdS and 10Ni₂P@CdS were estimated to be ca. 2.13, 2.28, 2.13 and 1.97 eV, respectively. This red shift in the optical absorption of samples could probably be attributed to the morphology differences of these samples. The narrow band gaps of the 10Ni₂P@CdS sample meant that they were able to be photoexcited to generate electron–hole pairs by visible light irradiation, thereby triggering chemical redox reactions. In addition, the variations in the band

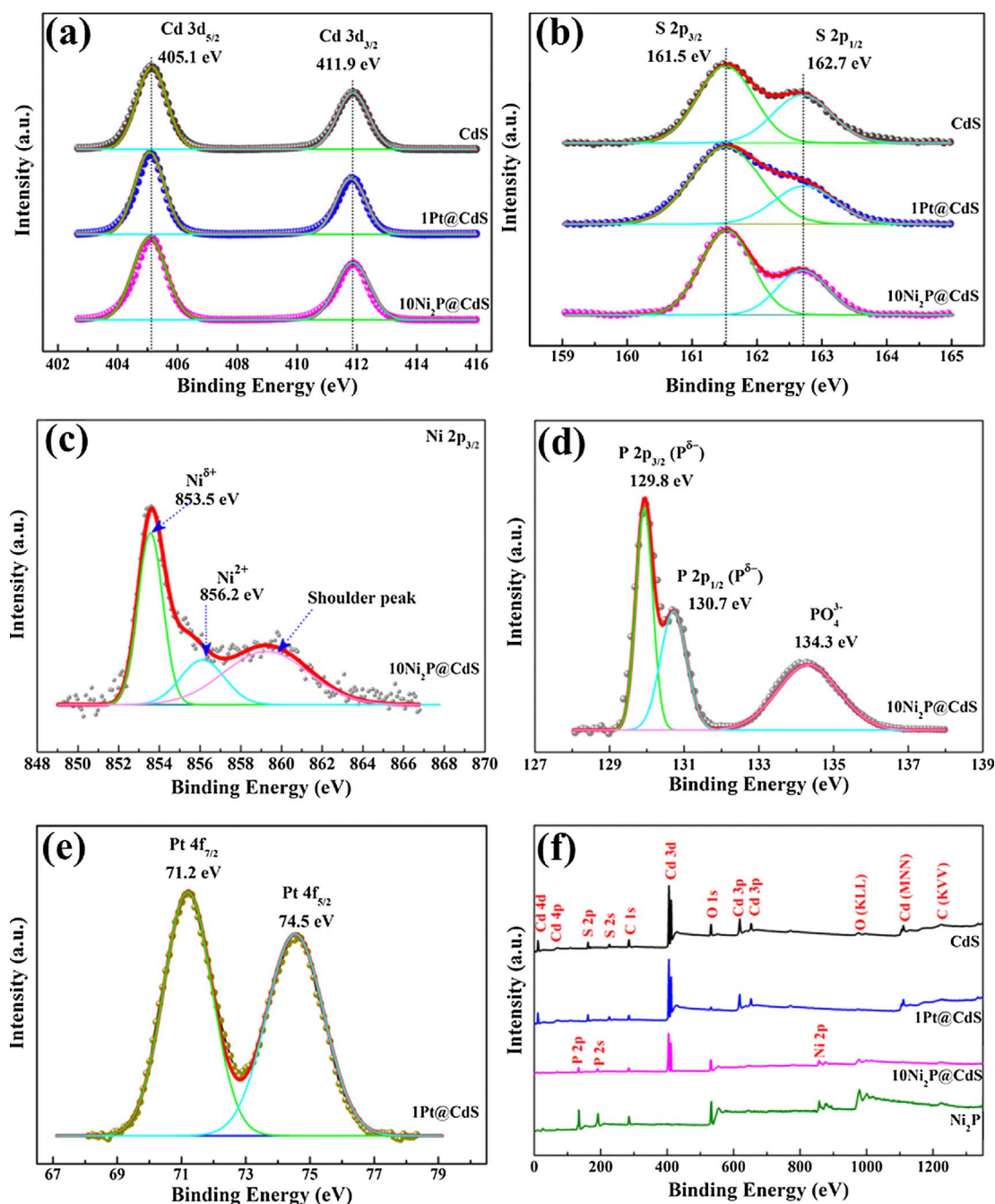


Fig. 4. (a) Cd 3d and (b) S 2p XPS spectra of CdS, 1Pt@CdS and 10Ni₂P@CdS samples; (c) Ni 2p_{3/2} and (d) P 2p XPS spectra of 10Ni₂P@CdS; (e) Pt 4f XPS spectra of 1Pt@CdS, and (f) XPS survey of CdS, Ni₂P, 1Pt@CdS and 10Ni₂P@CdS samples.

gap could probably cause a different degree of delocalization and mobility of photoexcited electron-hole pairs, which might then result in different photocatalytic efficiency [58]. For example, the band gaps of CdS and CdS-H were 2.13 and 2.28 eV, respectively, which further implied the photocatalytic activity of CdS was higher than that of CdS-H photocatalyst (see Fig. S2).

Mott-Schottky experiment was conducted to evaluate the band positions of the CdS, Ni₂P, 1Pt@CdS and 10Ni₂P@CdS samples in 0.5 mol/L Na₂SO₄ electrolyte (as shown in Fig. 8a). The positive slope of C^{-2} - E plot indicates that all samples in the nanocomposite are n-type semiconductors [56,59–61]. The flat-band potential (V_{fb}) of CdS was determined from extrapolation to the X intercept in the Mott-Schottky plot at various frequencies. It could be found that the introduction of Pt or Ni₂P had no effect on the band structure of CdS. The V_{fb} of CdS,

1Pt@CdS, 10Ni₂P@CdS and Ni₂P in the nanocomposite both approximately equaled -0.70 , -0.70 , -0.70 and -0.62 V vs SCE (-0.46 , -0.46 , -0.46 and -0.38 V vs NHE) [62]. It is known that the bottom of the conduction bands (CB) is more negative by -0.1 V than the flat band potential for many n-type semiconductors [63]. Furthermore, the band gap of Ni₂P is 1.0 eV in previous reference [45,64]. According to the band gap data, the estimated positions of CB and valence bands (VB) of four photocatalysts are given in Fig. 8b. It displays that the photocatalysts of CdS, 1Pt@CdS and 10Ni₂P@CdS are able to generate H₂ and O₂ by overall water splitting. Although the positions of CB or VB over 1Pt@CdS are similar to that of 10Ni₂P@CdS, its photoactivity is much lower than 10Ni₂P@CdS. This suggests that, in addition to the band positions, the charge transfer and fluorescence lifetime also plays a role in influencing photoactivity.

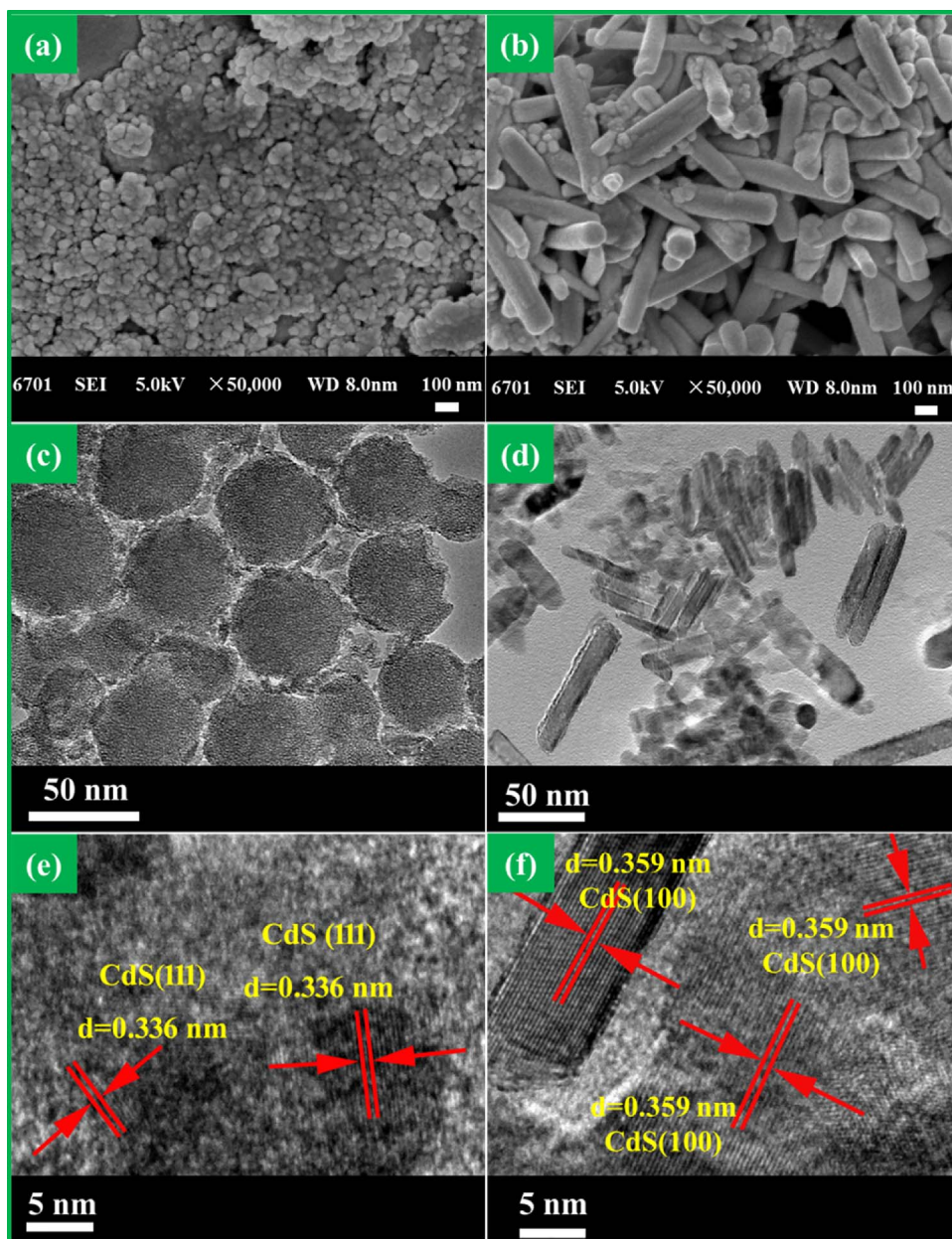
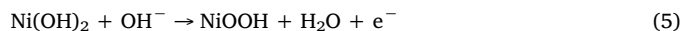


Fig. 5. SEM (a), TEM (c), and HRTEM (e) images of CdS sample; SEM (b), TEM (d), and HRTEM (f) images of CdS-H.

3.4. Electrochemical analysis

To further explore the role of Ni_2P in the $\text{Ni}_2\text{P}@\text{CdS}$, electrochemical analysis of the all samples has been carried out, including cyclic voltammetry (CV), transient photocurrent response, linear sweep voltammetry (LSV), Tafel Plots, electrochemical impedance spectroscopy (EIS) Nyquist plots, and open-circuit voltage response (V_{oc}) (as shown in Figs. 9 and 10). Fig. 9a gives the CV profiles of the $x\text{Ni}_2\text{P}@\text{CdS}$ ($x = 1, 2.5, 5, 10, 15$, and 20) electrode in the potential region of $0-0.8$ V at a scan rate of 1 mV s^{-1} . Note that $10\text{Ni}_2\text{P}@\text{CdS}$ exhibits much higher peak current density and a larger enclosed area compared with the other electrodes ($x = 1, 2.5, 5, 15$, and 20), implying the superior electrochemical activity of $10\text{Ni}_2\text{P}@\text{CdS}$. In Fig. 9b, the Ni_2P electrode displays the higher current density than other electrodes than that of CdS, $10\text{Ni}_2\text{P}@\text{CdS}$ and $1\text{Pt}@\text{CdS}$ electrodes at the same potential in 1 mol/L KOH electrolyte. The CV profile of Ni_2P shows a pair of redox peaks at 0.50 and 0.34 V (vs SCE). It can be ascribed to the redox reaction of $\text{Ni}^{2+}/\text{NiOOH}$ on the electrode surface in alkaline medium [65]. However, on the $10\text{Ni}_2\text{P}@\text{CdS}$ electrode surface, the oxidation

and reduction peaks shift to 0.47 and 0.39 V, respectively, indicating an irreversible oxidation and reduction reaction in KOH electrolyte [66]. Therefore, the surface Faradic reactions proceed according to the following reactions [67–69]:



In the beginning, Ni^{2+} ion in Ni_2P converts to $\text{Ni}(\text{OH})_2$ through an irreversible reaction (4). Meanwhile, the produced $\text{Ni}(\text{OH})_2$ further converts to NiOOH through the reversible reaction (5) at the same discharge condition.

The transient photocurrent–time curves of CdS, $1\text{Pt}@\text{CdS}$ and $x\text{Ni}_2\text{P}@\text{CdS}$ catalysts were measured by several on–off runs (Fig. 9c and d). It is easily to observe that the photocurrent over $10\text{Ni}_2\text{P}@\text{CdS}$ electrode is greatly improved compared with that of other electrodes. Because the photocurrent is formed mainly by the diffusion of photo-generated electrons to the back contact and simultaneously holes are taken up by the hole acceptor in the electrolyte [70], the enhanced

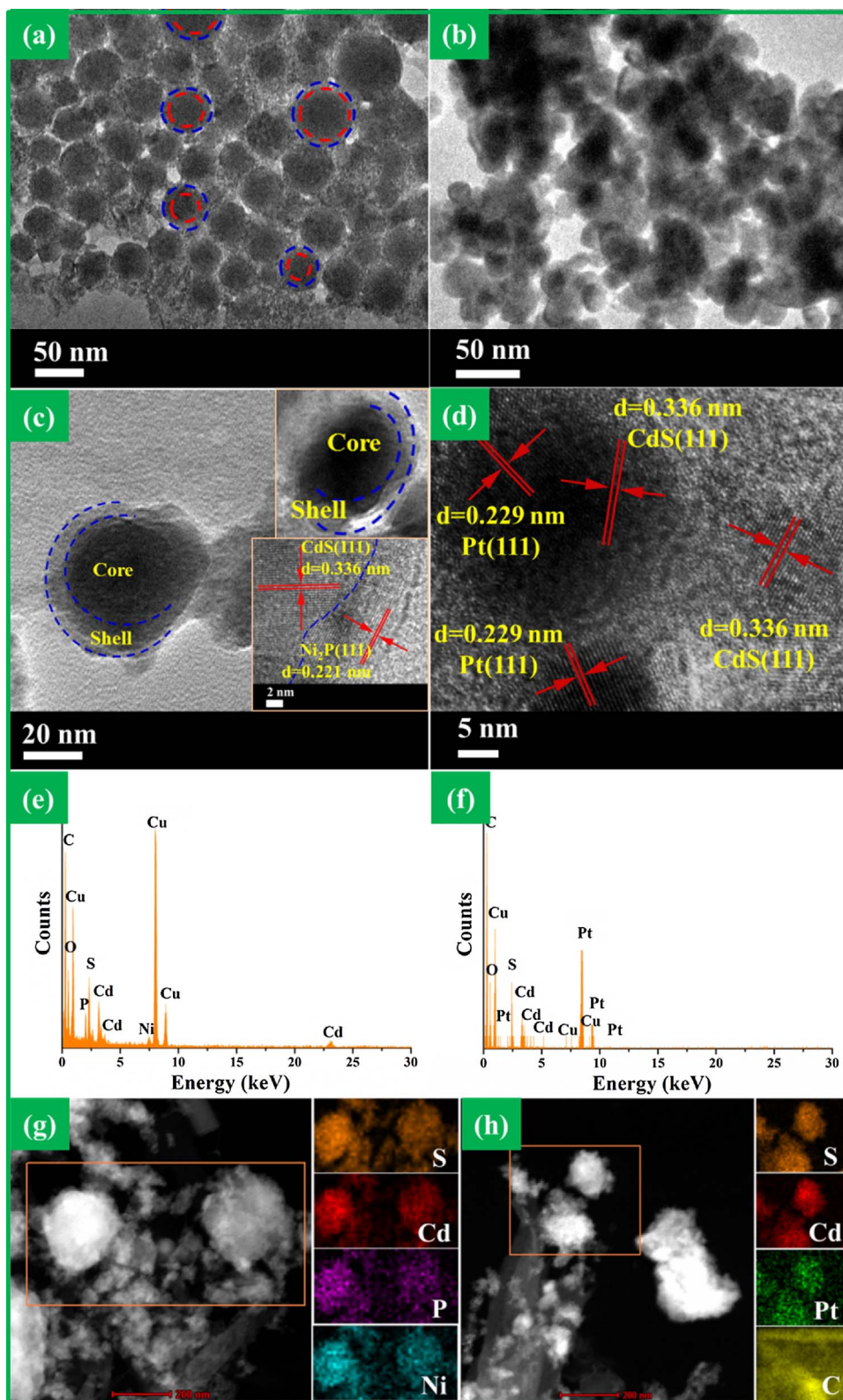


Fig. 6. TEM (a, b), HRTEM (c, d), EDX spectrum (e, f) and HAADF-STEM and EDX elemental mapping (g, h) images of 10Ni₂P@CdS and 1Pt@CdS.

photocurrent over the 10Ni₂P@CdS nanocomposite implies more efficient separation of the photoinduced electron-hole pairs and a longer lifetime of the photogenerated charge carriers than that of other electrodes, which is beneficial for its enhanced photocatalytic activity.

The electrochemical H₂ generation activities of CdS, Ni₂P, 1Pt@CdS and 10Ni₂P@CdS electrodes were also investigated by the LSV method. Fig. 10a gives the overpotential of different electrodes and shows that

compared with CdS (−0.53 V), Ni₂P (−0.38 V) and 1Pt@CdS (−0.34 V), 10Ni₂P@CdS had low overpotential (−0.32 V). Since the photocatalytic activity of HER is highly dependent on the overpotential of the HER reaction [71], further indicating 10Ni₂P@CdS is an excellent photocatalyst for HER. The low overpotential of 10Ni₂P@CdS might be due to the fast transfer of electrons. The results are consistent with the photocatalytic performance and photocurrent experiment. On the basis

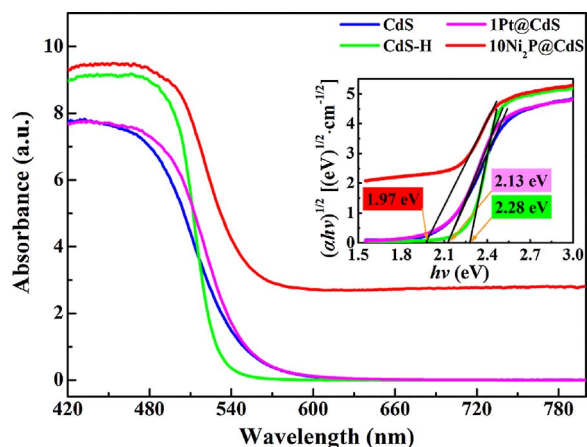


Fig. 7. The UV-vis diffuse reflectance spectra (DRS) of the CdS, CdS-H, 1Pt@CdS and 10Ni₂P@CdS samples; inset is the plot of transformed Kubelka-Munk function vs. the energy of light.

of the LSV curves, the corresponding Tafel plots were constructed (Fig. 10b). An important parameter to evaluate the activity in HER is the Tafel slope b , which is determined by fitting polarization data to the Tafel equation:

$$\eta = a + b \log |j| \quad (6)$$

Where η is the overpotential, b is the Tafel slope, and j is the current density. A smaller Tafel slope means a faster increase of HER rate with the increasing potential. The value of Tafel slope of the 10Ni₂P@CdS electrode is about 48 mV dec⁻¹, much lower than those of CdS (152 mV dec⁻¹), Ni₂P (82 mV dec⁻¹), and 1Pt@CdS (56 mV dec⁻¹), which further confirms the superior photocatalytic HER performance of 10Ni₂P@CdS. The low Tafel slope suggesting that hydrogen production takes place *via* the Volmer–Heyrovsky mechanism over the 10Ni₂P@CdS and 1Pt@CdS electrodes surface [72–74].

In addition, Fig. 10c displays the Nyquist plots of the EIS results cycled in 0.1 mol/L KOH electrolyte solution both exhibit semicircles at high frequencies. Considering that the preparation of the electrodes and electrolyte used are identical, the high frequency semicircle is relevant to the resistance of the electrodes [75]. In electrochemical spectra, the high-frequency arc corresponds to the charge transfer limiting process and can be attributed to the double-layer capacitance (C_{dl}) in parallel with the charge transfer resistance (R_{ct}) at the contact interface between the electrode and electrolyte solution [76,77]. In the Nyquist plots, the 10Ni₂P@CdS sample exhibited the smallest semicircle compared with 1Pt@CdS, CdS, and Ni₂P electrodes. Clearly, the introduction of Ni₂P nanoparticles leads to a significantly decreased diameter of

the semicircular Nyquist plot as compared to CdS, suggesting a faster charge transfer rate [75].

Fig. 10d shows a typical V_{oc} to illumination followed by termination of illumination. V_{oc} is defined as the difference in the Fermi levels between the photoanode (i.e. 10Ni₂P@CdS) and the counter electrodes. In the dark, the electrode potential is described by redox equilibration. Band gap excitation of CdS results in charge separation. As the holes are scavenged by hydroxyl species in the electrolyte at the interface, the electrons accumulation causes a shift in the Fermi levels to a more negative potentials and hence increasing the photovoltage under illumination, and we see an increase in V_{oc} . The V_{oc} reaches a maximum as the electron accumulation competes with the charge recombination and thus attains a steady state. Upon stopping the illumination, V_{oc} decays and the electrons accumulated undergo recombination [78–80].

3.5. Photoluminescence intensity and fluorescence lifetime analysis

Photoluminescence (PL) spectra could provide the information on trapping, migration, and recombination process of photogenerated electrons and holes, so it was performed to further clarify the photocatalytic mechanism. The high PL intensity manifested a high electron–hole recombination rate and poor photocatalytic performance [81]. The photoluminescence quenching of CdS, 1Pt@CdS and xNi₂P@CdS was examined (as shown in Fig. 11). In Fig. 11a, the PL spectra of xNi₂P@CdS under the excitation wavelength of 405 nm, and two distinct emission bands at about 470 and 541 nm can be observed. The emission peak at 470 nm is attributed to the band gap excitation, and the broad emission peak centered at 541 nm is due to surface emissions and possible metal vacancies (CdS), which is verified by the results from previous work [82]. In Fig. 11b, the PL spectra of CdS aqueous solution displayed a strong emission at 463 nm, which was caused by recombination of excited charge pairs bought on by exciting light. When Pt or Ni₂P was loaded in CdS, there was an obvious decrease of the peak intensity of the CdS emission; meanwhile, a slight red shift (~ 1 and 7 nm) of the emission peak was observed, respectively. This shift could be mainly ascribed to the interaction of CdS with Ni₂P over 10Ni₂P@CdS samples. The emission peaks at 528 and 541 nm is attributed to CdS surface vacancy defects. Furthermore, the PL intensity of 10Ni₂P@CdS is lower than that of other samples, illustrating that recombination rate of photogenerated electrons and holes is low.

In order to understand and retrieve quantitative insight about the photoinduced electron transfer mechanism in a CdS system, time-resolved photoluminescence (TRPL) spectroscopy measurement was performed on all samples (Fig. S5a–b). PL intensity decay, as a function of time, is monitored and the PL decay time is obtained by fitting the data in a two-exponential model using the following expression [83]:

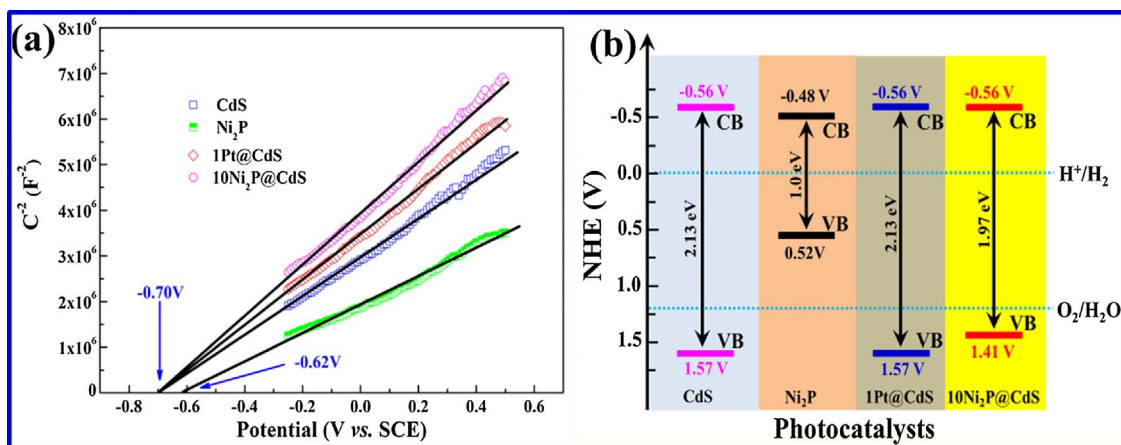


Fig. 8. (a) Mott-Schottky plots and (b) estimated band positions of the CdS, Ni₂P, 1Pt@CdS and 10Ni₂P@CdS photocatalysts in 0.5 mol/L Na₂SO₄ electrolytes.

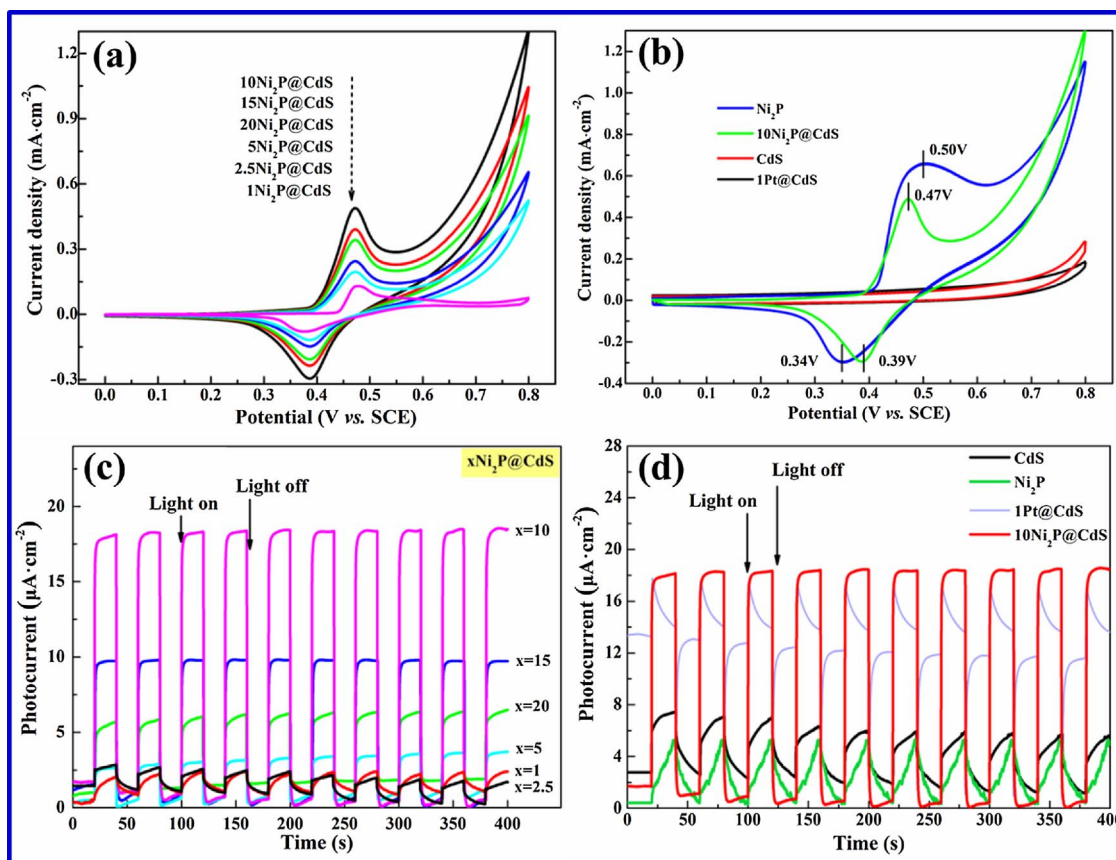


Fig. 9. Cyclic Voltammetry curves of (a) $x\text{Ni}_2\text{P}@/\text{CdS}$, and (b) CdS, Ni₂P, 1Pt@CdS and 10Ni₂P@CdS electrodes in the potential region of 0–0.8 V at a scan rate of 1 mV s⁻¹; Transient photocurrent response of (c) $x\text{Ni}_2\text{P}@/\text{CdS}$, and (d) CdS, Ni₂P, 1Pt@CdS and 10Ni₂P@CdS electrodes in 1 mol/L KOH aqueous solution.

$$I(t) = \sum_{i=1,2} B_i \exp(-t/\tau_i) \quad (7)$$

where I is the normalised emission intensity, t is the time after the pulsed laser excitation, B_i and τ_i are the amplitude (pre-exponential factor) and the PL decay time of the individual components, respectively. Fig. S5 exhibits that the lifetimes of 10Ni₂P@CdS is longer than that of other samples, indicating the effective electron transfer from CB of CdS to Ni₂P shell.

The average lifetime of two exponential decay is essential to describe the overall TRPL character [83,84], which is calculated using Eq. (8):

$$\langle \tau \rangle = \frac{\sum_{i=1,2} B_i \tau_i^2}{\sum_{i=1,2} B_i \tau_i} \quad (8)$$

where $\langle \tau \rangle$ is the average lifetime, B_i and τ_i are the amplitude (pre-exponential factor) and the PL decay time of the individual components, respectively. The fluorescence lifetimes were acquired by fitting the decay profiles with two exponential terms (see Tables Table 2 and S1). Apparently, the average lifetime of CdS, 1Pt@CdS and 10Ni₂P@CdS are 3.58, 4.59 and 16.27 ns, respectively. In fact, the $\langle \tau \rangle$ of 10Ni₂P@CdS is the longest among the $x\text{Ni}_2\text{P}@/\text{CdS}$ samples. These results further indicate the 10Ni₂P@CdS sample is more beneficial for electron transfer.

3.6. Isotopes tracer experiments, stability, ICP and AQE analysis

To further demonstrate that 10Ni₂P@CdS catalyst properties for water splitting under visible light irradiation, the isotopes tracer experiments were carried out. Fig. 12a displays the isotopes analysis results, illustrating the m/z signal at 4, corresponding to the D₂. Fig. 12b shows that the m/z signal at 2, 18, 20, 28, 32, 34, 36 and 40 are

attributed to H₂, H₂O (in air), H₂¹⁸O, N₂ (in air), ¹⁶O₂ (in air), ¹⁶O¹⁸O, ¹⁸O₂ and Ar, respectively. Trace amount of ¹⁶O¹⁸O formation might due to the oxygen atom exchange of H₂¹⁸O and ¹⁶O₂ (in air). In fact, the ¹⁶O¹⁸O formation is reasonable during isotopes experiments, which has already been investigated in the previous references [24,40]. The large amount of D₂ and ¹⁸O₂ evolution further proves that 10Ni₂P@CdS photocatalyst is able to overall water splitting.

To achieve effective hydrogen evolution via photocatalytic overall water splitting, the H₂ and O₂ recombination reaction must be inhibited [85,86]. Unfortunately, H₂ and O₂ recombination reverse reaction occurs very fast over photocatalyst surface. As shown in Fig. S6, the injected 2 mL H₂ and 4 mL O₂ recombine rapidly over 10Ni₂P@CdS and Ni₂P photocatalysts in a sealed Pyrex flask. Fig. S6a displays that the detected H₂ decreases significantly in the dark, indicating clear H₂ and O₂ recombination reaction. This result is in good agreement with the previous reference [26]. In the illumination, the amount of H₂ over 10Ni₂P@CdS has significantly increased after 30 min, which manifests that the rate of H₂ generation is higher than the recombination rate (as shown in Fig. S6b).

Furthermore, the stabilities of (a) 10Ni₂P@CdS (red balls), (b) Ni₂P (magenta balls), 1Pt@CdS (gray balls) and CdS (orange balls) photocatalysts were checked, and the results were shown in Fig. 13. It is observed that the 10Ni₂P@CdS exhibits excellent stability during the four cycles, the maximum amounts of H₂ evolution is 251.4 μmol (see Fig. 13a). In Fig. 13b, the CdS reveals low stability during the four cycles, which means that the loading Ni₂P can inhibit photocorrosion and promote stability of CdS. In Fig. S7, the used 10Ni₂P@CdS catalyst was characterized by XRD and XPS. As shown in Fig. S7a, it was found that the used 10Ni₂P@CdS catalyst had no significant difference between the fresh sample and the used sample on the crystal phase structure (see Fig. 3). In addition, XPS results further confirmed the

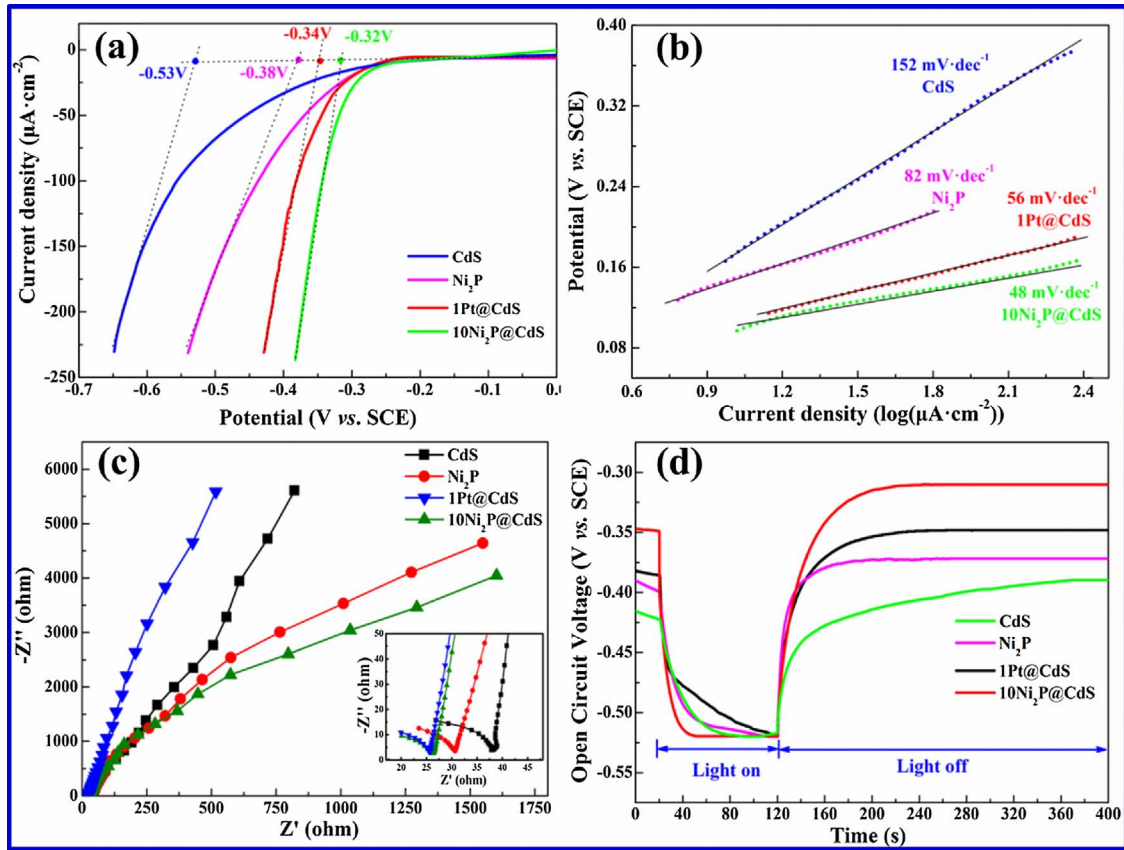


Fig. 10. Linear Sweep Voltammetry (a), Tafel Plots (b), electrochemical impedance spectroscopy (EIS) Nyquist plots (c), and open-circuit voltage response curves (d) of CdS, Ni₂P, 1Pt@CdS and 10Ni₂P@CdS electrodes in 1 mol/L KOH aqueous solution. The scan rate was 1 mV s⁻¹.

existence of Ni^{δ+}, P^{δ-}, Cd²⁺ and S²⁻ on the surface of the used 10Ni₂P@CdS sample (as shown in Fig. S7b–e). Fig. S7f showed XPS survey (wide-scan) spectra confirmed the existence of Cd, S, Ni and P elements over 10Ni₂P@CdS. The above results further suggested that the 10Ni₂P@CdS photocatalyst performed the excellent stability.

To further verify the Ni₂P can inhibit photocorrosion of CdS, we checked the Cd²⁺ concentration in the reaction solutions by ICP method for each run over CdS and 10Ni₂P@CdS reaction system, and the results were given in Fig. 14a. Obviously, the concentration of Cd²⁺ rise gradually with the increasing irradiation time for CdS sample, so the photocorrosion of CdS is indeed very serious in photocatalytic HER. But there is only negligible Cd²⁺ in the 10Ni₂P@CdS dispersion after

Table 2

The average fluorescence lifetimes of CdS, 1Pt@CdS and 10Ni₂P@CdS in pure H₂O; [Catalysts] = 0.5 mg/mL.

Samples	Lifetime, τ (ns)	Pre-exponential factors B	Average lifetime, <τ> (ns)	χ ²
CdS	τ ₁ = 0.298 τ ₂ = 4.843	B ₁ = 86.22 B ₂ = 13.78	3.58	1.103
1Pt@CdS	τ ₁ = 0.368 τ ₂ = 5.293	B ₁ = 70.48 B ₂ = 29.52	4.59	1.022
10Ni ₂ P@CdS	τ ₁ = 17.922 τ ₂ = 0.385	B ₁ = 17.08 B ₂ = 82.92	16.27	1.050

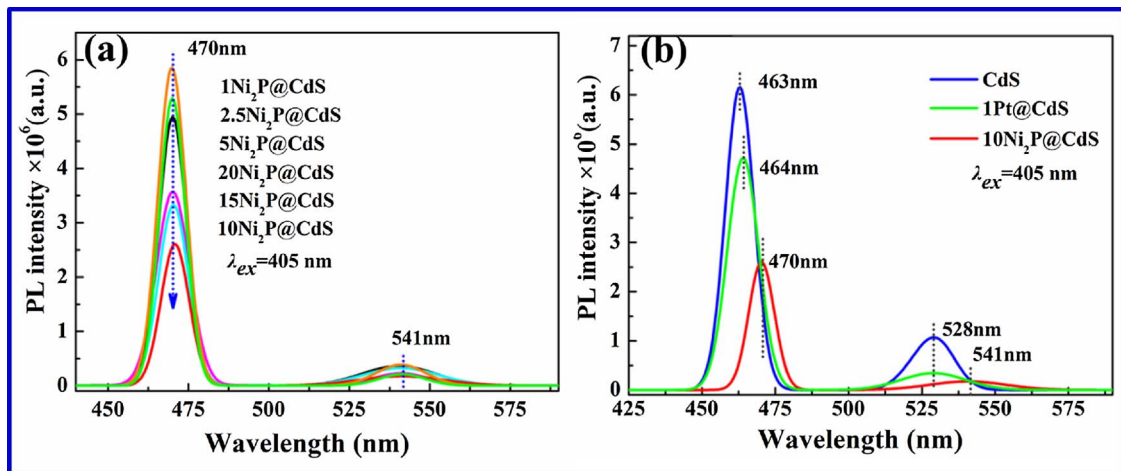


Fig. 11. Photoluminescence spectra of (a) xNi₂P₂@CdS and (b) CdS, 1Pt@CdS and 10Ni₂P@CdS samples in pure water at an excitation wavelength of 405 nm. [Catalysts] = 0.5 mg/mL.

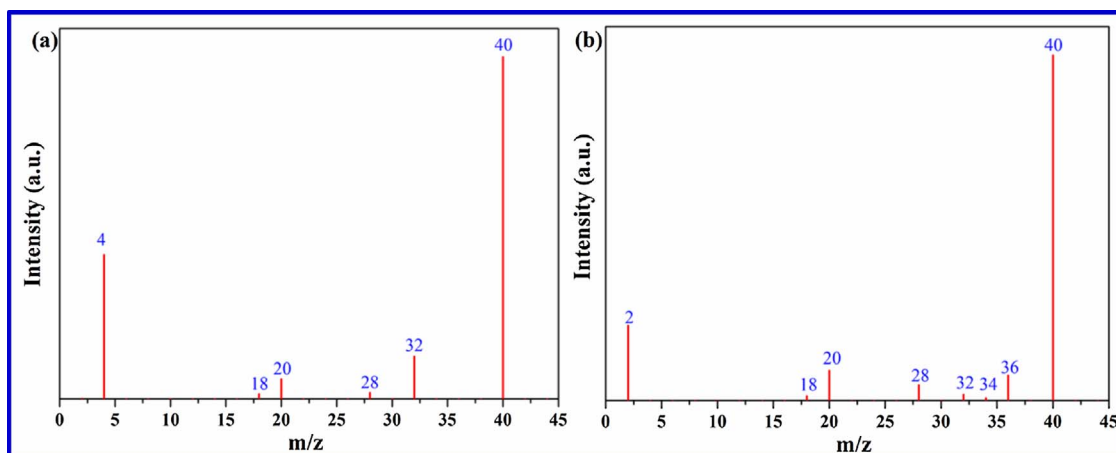


Fig. 12. GC-MS spectra obtained after injecting 0.5 mL samples of the gas phase species produced during illumination 6 h toward photocatalytic splitting over 10Ni₂P@CdS photocatalyst (a) D₂O and (b) H₂¹⁸O.

several cycles, far below than that of CdS sample.

To understand the concentration of S²⁻ ions in the 10Ni₂P@CdS dispersion solution, high sensitivity and selectivity fluorescent probe technology is used, due to the low concentration of S²⁻ in the reaction system. Specific testing procedures, methods and conditions are in accordance with the previous reference [87]. In Fig. S8a, upon the addition of S²⁻, the fluorescence intensity increases dramatically. The system exhibits significant quenching in the fluorescence intensity in the maximum emission at 469 nm under the excitation wavelength of 345 nm. Here, the “sample” represents the supernatant liquid after centrifugation of the 10Ni₂P@CdS photocatalytic system. Furthermore, the fluorescence intensities at 469 nm have an excellent linear relationship with the amount of S²⁻ from 0.03 to 0.09 μmol (as shown in Fig. S8b). The correlation coefficient R² of linear fitting is 0.9966. The fluorescence intensity of CuL+sample is 675 and the corresponding S²⁻-containing amount of sample is 0.03477 μmol. In other words, the 2 mL of the reaction mixture (sample) contained 0.03477 μmol S²⁻. It further means that the concentration of S²⁻ ions is 0.5563 ppm in the solution. The result is in good agreement with the photocatalytic activity, further demonstrates that excellent photocatalytic performance of 10Ni₂P@CdS is due to its efficient inhibition photocorrosion of CdS. In addition, to investigate the wavelength dependence of photocatalytic H₂ evolution, the AQE of 10Ni₂P@CdS and Ni₂P for hydrogen evolution were accomplished over a wide visible-light range of 430–550 nm. Fig. 14b exhibits that the highest AQE value of 10Ni₂P@CdS is 3.89% at 430 nm due to its higher potential of photon [88,89].

To further demonstrate the excellent performance the 10Ni₂P@CdS and other CdS-based photocatalysts. A detailed comparison of H₂-production rate in the CdS based photocatalysts via water splitting under visible light irradiation are shown in Table S2. Although the part of CdS-based catalysts showed the high HER activity and AQE, the noble metal Pt or sacrifice reagent was used in the reaction system. However, the noble metal and sacrifice reagent did not use in our work. The 10Ni₂P@CdS exhibited the excellent HER activity (837.94 μmol/h/g) and high AQE (3.89% at 430 nm), further confirming the outstanding photocatalytic behavior of 10Ni₂P@CdS photocatalyst.

As we know, it is very difficult for water oxidation (O₂ evolution) on CdS photocatalyst. In the case of aqueous CdS suspension, photouptake of oxygen is an efficient process which is expected to remove rapidly any oxygen produced from the reaction of valence band holes with water. This reaction leads to dissolution of the CdS particles whereby H₂O₂ and sulfate are formed simultaneously [90]. To produce hydrogen efficiently on CdS photocatalytic system, the O₂ should be removed to the outside of the reaction system. The application of artificial gill in photocatalytic overall water splitting might remove neonatal formed O₂ from water and prevent the oxygen leading photocorrosion [40].

In Fig. S9a, only the addition of electron scavenger KBrO₃ leading to trace of the oxygen was produced over CdS [91]. Furthermore, the O₂ evolution remarkably improved with the help of artificial gill in the KBrO₃ aqueous solution under visible-light irradiation. Apparently, the water oxidation (O₂ evolution) is achievable under the electron scavenger and artificial gill over CdS. Fig. S9b shows the H₂/O₂-production

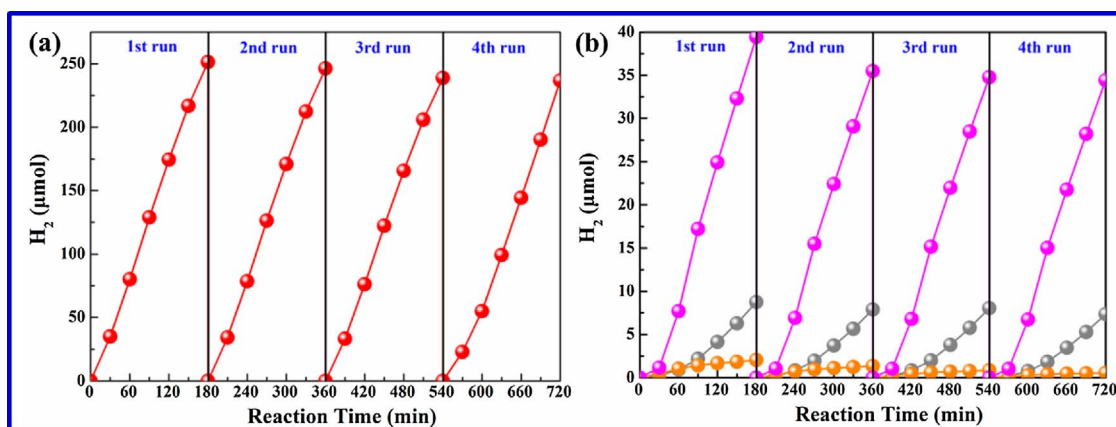


Fig. 13. Stability tests of hydrogen evolution for (a) 10Ni₂P@CdS (red balls), (b) Ni₂P (magenta balls), 1Pt@CdS (gray balls) and CdS (orange balls) photocatalysts under visible light irradiation. The reaction continued for 12 h, with evacuation every 3 h. After every run, the reaction system was replaced by Ar gas. (For interpretation of the references to colour in this figure legend, the reader is referred to the web version of this article.)

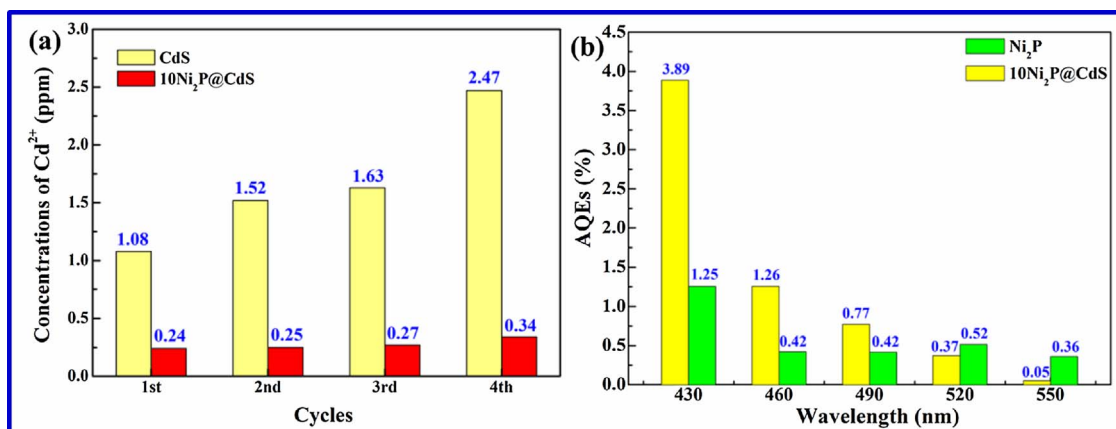


Fig. 14. (a) The concentration of Cd²⁺ for each run in the reaction solution of CdS and 10Ni₂P@CdS under visible light irradiation and (b) AQE of hydrogen evolution systems of Ni₂P and 10Ni₂P@CdS in 150 mL of pure H₂O at different wavelengths.

over 10Ni₂P@CdS photocatalyst with artificial gill. 142.8 μmol of O₂ is evolved over the 10Ni₂P@CdS in 180 min, which is close to half of H₂ production.

In order to understand the active sites of hydrogen production and oxygen production over 10Ni₂P@CdS, the following is discussed in detail. As shown in Fig. S10a, O₂ cannot be generated over Ni₂P surface when the hole in CdS transfer to the VB of Ni₂P. Because the VB energy positions of Ni₂P is lower than the potentials of oxygen evolution (1.23 V). In fact, the 10Ni₂P@CdS photocatalyst exhibit excellent photocatalytic oxygen production performance in Fig. S10b. Therefore, the path of hole-transferring from CdS to Ni₂P is unreasonable. Moreover, the hydrogen generation can be achieved over the Ni₂P surface. So, it is reasonable that the electron in CdS transfers to the CB of Ni₂P (see Fig. S10b). The photocatalytic HER and oxygen production process over 10Ni₂P@CdS catalyst under the visible light irradiation could be depicted in Fig. S10c. Ni₂P served as both effective capture site to accept the photogenerated electrons and the reduction active site of proton to H₂. H₂O is oxidized by the hole of CdS generation amount oxygen.

Hydroxyl radicals (·OH) is commonly suggested as the primary oxidizing species in photocatalytic process [92]. To interpret the photocatalytic performances observed over prepared 10Ni₂P@CdS sample, the generation and evolution of oxygen-containing species with irradiation time were probed by EPR technique with DMPO (dimethyl pyridineN-oxide) as a spin trapping agent. Fig. 15 shows the EPR signals of DMPO··OH on 10Ni₂P@CdS photocatalyst. Clearly, no signals of ·OH adducts can be detected in the dark under an atmosphere of Ar. After a 2 min illumination, the characteristic quartet peaks of the DMPO··OH adduct with intensity ratio ca. 1:2:2:1 can be observed for the water-suspended 10Ni₂P@CdS sample, which is consistent with the reported spectra [93]. Our EPR results suggest that the ·OH is really formed during the photocatalytic water splitting for 10Ni₂P@CdS sample.

3.7. Photocatalytic mechanism for H₂ evolution over 10Ni₂P@CdS

The photocatalytic HER mechanism of 10Ni₂P@CdS catalyst under the visible light irradiation could be depicted in Scheme 2. Band gap excitation of CdS results in charge separation. The CB electron of CdS is transferred into the shell of Ni₂P. The shell of Ni₂P served as both effective capture site to accept the photogenerated electrons and the reduction active site of proton to H₂. H₂O is oxidized by the VB hole of CdS generation amount oxygen, and then the O₂ is removed to the outside of the reaction system through artificial gill. The artificial gill not only removes newly formed O₂ from water to prevent the oxygen leading photocorrosion, but probably inhibits the hydrogen and oxygen back recombination to water. Therefore, the 10Ni₂P@CdS catalyst

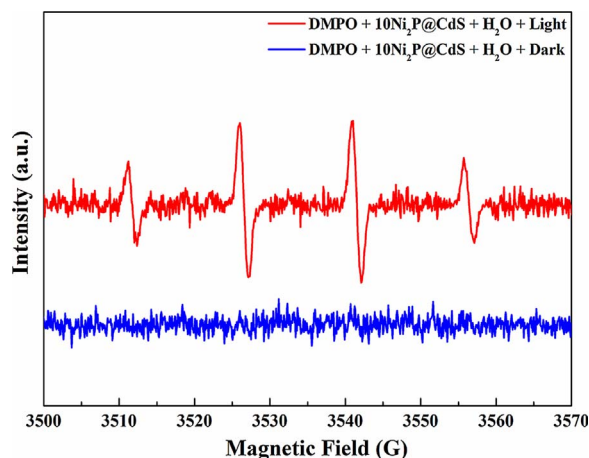


Fig. 15. Typical EPR spectra for photocatalytic splitting H₂O on 10Ni₂P@CdS in the presence of DMPO as an electron trapping agent. The signals were collected under light irradiation. Without light irradiation, no signal was detected. Conditions: catalyst concentrations, 0.1 mg mL⁻¹; DMPO, 5 mmol L⁻¹; in argon; irradiation time, 2 min; test temperature, 298 K; light Source: 300 W Xe lamp.

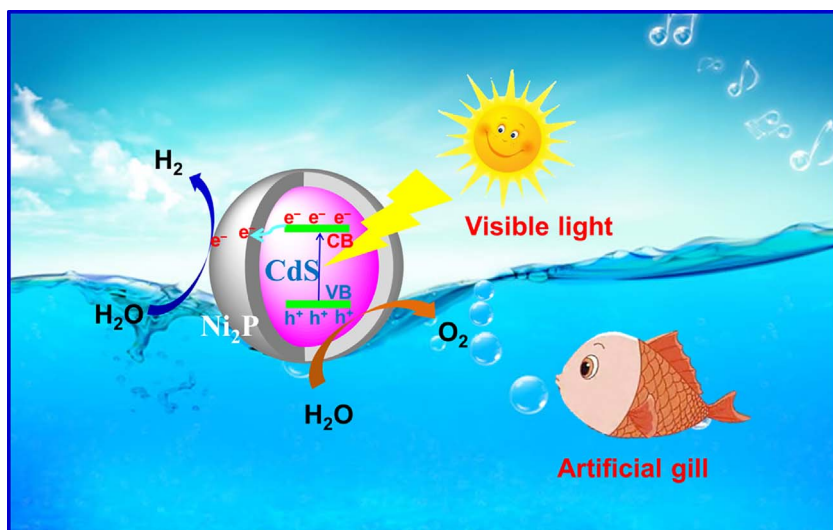
exhibited high activity for hydrogen formation from water under visible illumination.

4. Conclusions

In summary, we synthesized core-shell structured Ni₂P@CdS photocatalyst by solvothermal method for high efficient water splitting under visible light irradiation without sacrifice reagent and noble metal loading. Applying artificial gill to remove newly formed O₂ from water clearly prevent the oxygen leading CdS photocorrosion and inhibit the hydrogen and oxygen recombination back to water. Compared with CdS, the 10Ni₂P@CdS photocatalyst exhibits excellent photocatalytic performance (251.4 μmol of H₂ in 180 min) with high AQE (3.89% at 430 nm), in the meantime, it present high photocurrent, low overpotential (−0.32 V vs SCE), and long fluorescence lifetime (16.27 ns) of excited charges. ICP results further indicated the Ni₂P shell role on anti-photocorrosion of CdS surface. The photocatalytic H₂ evolution activity and stability of 10Ni₂P@CdS are superior to that of 1Pt@CdS (8.7 μmol in 180 min). Ni₂P is an excellent co-catalyst for semiconductor photocatalytic overall water splitting.

Notes

The authors declare no competing financial interest.



Scheme 2. Mechanism of overall water splitting over 10Ni₂P@CdS under visible illumination and artificial gill.

Acknowledgments

The authors are thankful for the support of the NSFC (Grant Nos. 21373245 and 21433007).

Appendix A. Supplementary data

Supplementary data associated with this article can be found, in the online version, at <http://dx.doi.org/10.1016/j.apcatb.2017.09.024>.

References

- [1] M.S. Dresselhaus, I.L. Thomas, *Nature* 414 (2001) 332–337.
- [2] Z. Han, F. Qiu, R. Eisenberg, P.L. Holland, T.D. Krauss, *Science* 338 (2012) 1321–1324.
- [3] N. Zhang, M.-Q. Yang, S. Liu, Y. Sun, Y.-J. Xu, *Chem. Rev.* 115 (2015) 10307–10377.
- [4] L. Fang, X. Wang, Y. Li, P. Liu, Y. Wang, H. Zeng, H. Yang, *Appl. Catal. B* 200 (2017) 578–584.
- [5] Q. Lu, C. Li, F. Wang, Q. Ren, Z. Ren, *J. Mol. Catal. (China)* 30 (2016) 557–565.
- [6] S.U.M. Khan, M. Al-Shahry, W.B. Ingler, *Science* 297 (2002) 2243–2245.
- [7] D. Wang, Y. Liu, C. Wang, F. Zhou, W. Liu, *ACS Nano* 3 (2009) 1249–1257.
- [8] P. He, Y. Chen, W. Fu, *J. Mol. Catal. (China)* 30 (2016) 69–275.
- [9] A. Kudo, Y. Miseki, *Chem. Soc. Rev.* 38 (2009) 253–278.
- [10] X. Chen, S. Shen, L. Guo, S.S. Mao, *Chem. Rev.* 110 (2010) 6503–6570.
- [11] C. Wu, Y. Fang, P. Zhao, J. Yang, M. Jia, Y. Huang, *J. Mol. Catal. (China)* 29 (2015) 369–381.
- [12] S.S.K. Ma, T. Hisatomi, K. Maeda, Y. Moriya, K. Domen, *J. Am. Chem. Soc.* 134 (2012) 19993–19996.
- [13] Z. Li, Y. Wu, G. Lu, *Appl. Catal. B* 188 (2016) 56–64.
- [14] X. Wang, K. Maeda, A. Thomas, K. Takanabe, G. Xin, J.M. Carlsson, K. Domen, M. Antonietti, *Nat. Mater.* 8 (2009) 76–80.
- [15] F. Jiang, Gunawan, T. Harada, Y. Kuang, T. Minegishi, K. Domen, S. Ikeda, *J. Am. Chem. Soc.* 137 (2015) 13691–13697.
- [16] M. Wang, L. Cai, Y. Wang, F. Zhou, K. Xu, X. Tao, Y. Chai, *J. Am. Chem. Soc.* 139 (2017) 4144–4151.
- [17] T. Inoue, A. Fujishima, S. Konishi, K. Honda, *Nature* 277 (1979) 637–638.
- [18] A. Kudo, Y. Miseki, *Chem. Soc. Rev.* 38 (2009) 253–278.
- [19] C. Wang, L. Wang, J. Jin, J. Liu, Y. Li, M. Wu, L. Chen, B. Wang, X. Yang, B.-L. Su, *Appl. Catal. B* 188 (2016) 351–359.
- [20] K. Ikeue, S. Shiiba, M. Machida, *Chem. Mater.* 22 (2010) 743–745.
- [21] Y. Hu, X. Gao, L. Yu, Y. Wang, J. Ning, S. Xu, X.W. Lou, *Angew. Chem. Int. Ed.* 52 (2013) 5636–5639.
- [22] M. Yang, C. Han, Y. Xu, *J. Phys. Chem. C* 119 (2015) 27234–27246.
- [23] D. Meissner, R. Memming, B. Kastening, *J. Phys. Chem.* 92 (1988) 3476–3483.
- [24] W. Gao, W. Zhang, G. Lu, *Appl. Catal. B* 212 (2017) 23–31.
- [25] C. Pan, T. Takata, M. Nakabayashi, T. Matsumoto, N. Shibata, Y. Ikuhara, K. Domen, *Angew. Chem. Int. Ed.* 54 (2015) 2955–2959.
- [26] Z. Li, B. Tian, W. Zhen, Y. Wu, G. Lu, *Appl. Catal. B* 203 (2017) 408–415.
- [27] H. Yan, J. Yang, G. Ma, G. Wu, X. Zong, Z. Lei, J. Shi, C. Li, *J. Catal.* 266 (2009) 165–168.
- [28] N. Ji, T. Zhang, M. Zheng, A. Wang, H. Wang, X. Wang, J.G. Chen, *Angew. Chem. Int. Ed.* 47 (2008) 8510–8513.
- [29] E.J. Popczun, C.G. Read, C.W. Roske, N.S. Lewis, R.E. Schaak, *Angew. Chem. Int. Ed.* 53 (2014) 5427–5430.
- [30] J. Tian, Q. Liu, N. Cheng, A.M. Asiri, X. Sun, *Angew. Chem. Int. Ed.* 53 (2014) 9577–9581.
- [31] E.J. Popczun, J.R. McKone, C.G. Read, A.J. Baciocchi, A.M. Wiltout, N.S. Lewis, R.E. Schaak, *J. Am. Chem. Soc.* 135 (2013) 9267–9270.
- [32] J. Tian, Q. Liu, A.M. Asiri, X. Sun, *J. Am. Chem. Soc.* 136 (2014) 7587–7590.
- [33] C. Wang, J. Jiang, X. Zhou, W. Wang, J. Zuo, Q. Yang, *J. Power Sources* 286 (2015) 464–469.
- [34] R.B. Levy, M. Boudart, *Science* 181 (1973) 547–549.
- [35] Z. Xing, Q. Liu, A.M. Asiri, X. Sun, *Adv. Mater.* 26 (2014) 5702–5707.
- [36] M.C. Liu, D.W. Jing, Z.H. Zhou, L.J. Guo, *Nat. Commun.* 4 (2013) 2278.
- [37] Y. Xie, H. Su, X. Qian, X. Liu, Y. Qian, *J. Solid State Chem.* 149 (2000) 88–91.
- [38] Z. Sun, H. Zheng, J. Li, P. Du, *Energy Environ. Sci.* 8 (2015) 2668–2676.
- [39] W. Zhen, B. Li, G. Lu, J. Ma, *Chem. Commun.* 51 (2015) 1728–1731.
- [40] X. Ning, J. Li, B. Yang, W. Zhen, Z. Li, B. Tian, G. Lu, *Appl. Catal. B* 212 (2017) 129–139.
- [41] Y. Xu, R. Wu, J. Zhang, Y. Shi, B. Zhang, *Chem. Commun.* 49 (2013) 6656–6658.
- [42] X. Ning, S. Meng, X. Fu, X. Ye, S. Chen, *Green Chem.* 18 (2016) 3628–3639.
- [43] Q. Xiang, B. Cheng, J. Yu, *Appl. Catal. B* 138–139 (2013) 299–303.
- [44] J. Chang, L. Feng, C. Liu, W. Xing, X. Hu, *Angew. Chem. Int. Ed.* 53 (2014) 122–126.
- [45] A. Panneerselvam, M.A. Malik, M. Afzaal, P. O'Brien, M. Helliwell, *J. Am. Chem. Soc.* 130 (2008) 2420–2421.
- [46] H. Li, Z. Bian, J. Zhu, Y. Huo, H. Li, Y. Lu, *J. Am. Chem. Soc.* 129 (2007) 4538–4539.
- [47] Z. Bian, T. Tachikawa, W. Kim, W. Choi, T. Majima, *J. Phys. Chem. C* 116 (2012) 25444–25453.
- [48] D.H. Wang, L. Wang, A.W. Xu, *Nanoscale* 4 (2012) 2046–2053.
- [49] G. Yang, B. Yang, T. Xiao, Z. Yan, *Appl. Surf. Sci.* 283 (2013) 402–410.
- [50] J.A. Cecilia, A. Infantes-Molina, E. Rodríguez-Castellón, A. Jiménez-López, S.T. Oyama, *Appl. Catal. B* 136–137 (2013) 140–149.
- [51] Z. Zhang, S. Liu, J. Xiao, S. Wang, *J. Mater. Chem. A* 4 (2016) 9691–9699.
- [52] M. Ledendecker, S.K. Calderón, C. Papp, H.-P. Steinrück, M. Antonietti, M. Shalom, *Angew. Chem. Int. Ed.* 54 (2015) 12361–12365.
- [53] N. Jiang, B. You, M. Sheng, Y. Sun, *Angew. Chem. Int. Ed.* 54 (2015) 6251–6254.
- [54] K. Zhou, W.J. Zhou, L.J. Yang, J. Lu, S. Cheng, W.J. Mai, Z.H. Tang, L.G. Li, S.W. Chen, *Adv. Funct. Mater.* 25 (2015) 7530–7538.
- [55] J.A. Cecilia, A. Infantes-Molina, J. Sanmartín-Donoso, E. Rodríguez-Aguado, D. Ballesteros-Plata, E. Rodríguez-Castellón, *Catal. Sci. Technol.* 6 (2016) 7323–7333.
- [56] N. Zhang, S. Liu, X. Fu, Y.-J. Xu, *J. Mater. Chem.* 22 (2012) 5042–5052.
- [57] D.V. Talapin, R. Koeppel, S. Götzinger, A. Kornowski, J.M. Lupton, A.L. Rogach, O. Benson, J. Feldmann, H. Weller, *Nano Lett.* 3 (2003) 1677–1681.
- [58] Y. Zhang, N. Zhang, Z.-R. Tang, Y.-J. Xu, *Chem. Sci.* 3 (2012) 2812–2822.
- [59] D.-S. Kong, *Langmuir* 24 (2008) 5324–5331.
- [60] X. Yang, A. Wolcott, G. Wang, A. Sobo, R.C. Fitzmorris, F. Qian, J.Z. Zhang, Y. Li, *Nano Lett.* 9 (2009) 2331–2336.
- [61] X. Xiao, J. Jiang, L. Zhang, *Appl. Catal. B* 142–143 (2013) 487–493.
- [62] M.W. Kanan, D.G. Nocera, *Science* 321 (2008) 1072–1075.
- [63] A. Ishikawa, T. Takata, J.N. Kondo, M. Hara, H. Kobayashi, K. Domen, *J. Am. Chem. Soc.* 124 (2002) 13547–13553.
- [64] M. Sharon, G. Tamizhmani, *Sol. Cells* 26 (1989) 303–312.
- [65] Q.-Q. Sun, M. Wang, S.-J. Bao, Y. Wang, S. Gu, *Analyst* 141 (2016) 256–260.
- [66] Y. Lu, J. Liu, X. Liu, S. Huang, T. Wang, X. Wang, C. Gu, J. Tu, S.X. Mao, *CrystEngComm* 15 (2013) 7071–7079.
- [67] R.K. Shervedani, A. Lasia, *J. Electrochem. Soc.* 144 (1997) 511–519.
- [68] C.-C. Hu, C.-Y. Cheng, *J. Power Sources* 111 (2002) 137–144.
- [69] C. An, Y. Wang, Y. Wang, G. Liu, L. Li, F. Qiu, Y. Xu, L. Jiao, H. Yuan, *RSC Adv.* 3 (2013) 4628–4633.
- [70] S. Soedergren, A. Hagfeldt, J. Olsson, S.-E. Lindquist, *J. Phys. Chem.* 98 (1994) 5552–5556.

- [71] H. Ezaki, M. Morinaga, S. Watanabe, *Electrochim. Acta* 38 (1993) 557–564.
- [72] S. Peng, L. Li, X. Han, W. Sun, M. Srinivasan, S.G. Mhaisalkar, F. Cheng, Q. Yan, J. Chen, S. Ramakrishna, *Angew. Chem. Int. Ed.* 53 (2014) 12594–12599.
- [73] X. Zhou, Y. Liu, H. Ju, B. Pan, J. Zhu, T. Ding, C. Wang, Q. Yang, *Chem. Mater.* 28 (2016) 1838–1846.
- [74] X. Huang, C. Tan, Z. Yin, H. Zhang, *Adv. Mater.* 26 (2014) 2185–2204.
- [75] D. Wang, D. Choi, J. Li, Z. Yang, Z. Nie, R. Kou, D. Hu, C. Wang, L.V. Saraf, J. Zhang, I.A. Aksay, J. Liu, *ACS Nano* 3 (2009) 907–914.
- [76] T. Lu, Y. Zhang, H. Li, L. Pan, Y. Li, Z. Sun, *Electrochim. Acta* 55 (2010) 4170–4173.
- [77] H.-L. Guo, X.-F. Wang, Q.-Y. Qian, F.-B. Wang, X.-H. Xia, *ACS Nano* 3 (2009) 2653–2659.
- [78] B.H. Meekins, P.V. Kamat, *ACS Nano* 3 (2009) 3437–3446.
- [79] R.P. Antony, P.S. Bassi, F.F. Abdi, S.Y. Chiam, Y. Ren, J. Barber, J.S.C. Loo, L.H. Wong, *Electrochim. Acta* 211 (2016) 173–182.
- [80] F.X. Xiao, S.F. Hung, J. Miao, H.Y. Wang, H. Yang, B. Liu, *Small* 11 (2015) 554–567.
- [81] D. Xu, W. Shi, C. Song, M. Chen, S. Yang, W. Fan, B. Chen, *Appl. Catal. B* 191 (2016) 228–234.
- [82] A.B. Panda, G. Glaspell, M.S. El-Shall, *J. Am. Chem. Soc.* 128 (2006) 2790–2791.
- [83] Q. Zeng, X. Kong, Y. Sun, Y. Zhang, L. Tu, J. Zhao, H. Zhang, *J. Phys. Chem. C* 112 (2008) 8587–8593.
- [84] H. Chauhan, Y. Kumar, J. Dana, B. Satpati, H.N. Ghosh, S. Dekka, *Nanoscale* 8 (2016) 15802–15812.
- [85] Y.H. Li, J. Xing, Z.J. Chen, Z. Li, F. Tian, L.R. Zheng, H.F. Wang, P. Hu, H.J. Zhao, H.G. Yang, *Nat. Commun.* 4 (2013) 2500.
- [86] Y.-J. Cho, G. Moon, T. Kanazawa, K. Maeda, W. Choi, *Chem. Commun.* 52 (2016) 9636–9639.
- [87] X. Yao, Y. Guo, J. Ru, C. Xu, Y. Liu, W. Qin, G. Zhang, X. Tang, W. Liu, *Sens. Actuators B: Chem.* 198 (2014) 20–25.
- [88] C. Kong, S. Min, G. Lu, *Int. J. Hydrogen Energy* 39 (2014) 4836–4844.
- [89] S. Min, G. Lu, *J. Phys. Chem. C* 115 (2011) 13938–13945.
- [90] N.M. Dimitrijević, S. Li, M. Grätzel, *J. Am. Chem. Soc.* 106 (1984) 6565–6569.
- [91] M. Muruganandham, M. Swaminathan, *J. Hazard. Mater.* 135 (2006) 78–86.
- [92] X. Fu, D. Huang, Y. Qin, L. Li, X. Jiang, S. Chen, *Appl. Catal. B.* 148–149 (2014) 532–542.
- [93] R. Li, Y. Weng, X. Zhou, X. Wang, Y. Mi, R. Chong, H. Han, C. Li, *Energy Environ. Sci.* 8 (2015) 2377–2382.